# Rapid heat discharge during deep-sea eruptions generates megaplumes and disperses tephra

Samuel S. Pegler[1] and David J. Ferguson[2]

**Deep-marine volcanism drives Earth's most energetic transfers of heat and mass between the crust and the oceans. Magmatic activity on the seafloor has been correlated in time with the appearance of massive enigmatic plumes of hydrothermal fluid known as megaplumes, yet little is known of the primary source and intensity of the hydrothermal energy release that occurs during seafloor volcanic events. Consequently, the origin of megaplumes remains ambiguous. By developing a mathematical model for the dispersal of submarine tephras, we show that the transport of pyroclasts requires an energy discharge that is sufficiently powerful ($\sim$1-2 TW) to form a hydrothermal plume with characteristics matching those of observed megaplumes in a matter of hours. Our results imply a direct link between megaplume creation, active magma extrusion and tephra dispersal. The energy flux required at the plume source is difficult to attain by purely volcanogenic means, and likely requires an additional input of heat, potentially from rapid evacuation of hot hydrothermal fluids triggered by dyke intrusion. In view of the ubiquity of submarine tephra deposits, our results suggest that short intervals of rapid hydrothermal discharge are commonplace during deep-ocean volcanism.**

## INTRODUCTION

### Deep-marine volcanism and megaplumes

The vast majority of Earth's volcanism occurs underwater in the deep oceans ($>$500 m water depths), mostly at ocean ridges and seamounts. Submarine magmatism accounts for $>$80% of the global volcanic heat flux [1] and facilitates important chemical-physical interactions between the crust and the oceans via seafloor hydrothermal activity. A significant, but poorly understood, aspect of this hydrothermal activity is the generation of massive (10-150 km$^3$) ephemeral emissions of hydrothermal fluid known as 'megaplumes' (or large-volume 'event plumes') [2–7] (Fig. 1). Megaplumes are characterized by high ratios of heat to hydrothermal chemical components compared to the plumes produced by chronic hydrothermal vents [7],

---

[1] School of Mathematics, University of Leeds, Leeds, LS2 9JT, UK. Email: s.pegler@leeds.ac.uk
[2] School of Earth and Environment, University of Leeds, Leeds, LS2 9JT, UK. Email: d.j.ferguson@leeds.ac.uk

such as black smokers. Their total energy contents are within the range $\sim 10^{16} - 10^{17}$ J, comparable to the annual thermal output from a typical mid-ocean ridge (MOR) hydrothermal vent field [2] and implying extremely high rates of energy discharge. The detection of megaplumes along MORs by physico-chemical measurements in the water column has occurred both fortuitously during pre-planned surveys [2, 3, 8] and during rapid response cruises undertaken following the detection of geophysical evidence for submarine eruptions [9, 10], such as seismic or hydrophone activity (see [5] for a review). Subsequent ocean floor surveys, when conducted, have provided evidence for contemporaneous eruptive activity [4, 11] and megaplume creation appears to be linked in space and time with deep sea volcanic events [5]. Observed concentrations of labile chemical species in megaplume fluids, such as $H_2$ [12] and dissolved Fe [13], generally indicate that the period of hydrothermal discharge was relatively brief and that megaplume formation is likely an ephemeral processes, probably associated with transient magmatic events. Despite the apparent link with active volcanism, the processes that form a megaplume remain unclear. Several theories exist for the source(s) of megaplume heat contents and fluids. These include: a purely volcanic origin via heat transfer from erupted lava and volatiles [14, 15]; a magmatic origin due to heating of pore fluids by intruded magma in a dyke [16]; or a hydrothermal origin via the rapid evacuation of existing intracrustal fluid reservoirs [2, 7]. Differentiating between these is challenging because few observations of active deep marine eruptions exist. In particular, while models of the dynamics of megaplumes have suggested they form rapidly [17], little is known of the rates of energy or volume discharge feeding the plume during a seafloor eruption, of the primary source of the hydrothermal input, nor of the role of eruption dynamics on plume formation.

To address these questions, we develop a model of tephra transport in the neutrally buoyant umbrella of a hydrothermal plume, determine constraints on the energetics of syn-eruptive heat discharge during deep submarine eruptions and establish a conclusive link between tephra producing eruptions and megaplume creation. Our model enables a novel methodology of using buoyancy-driven tephra transport by the umbrella of volcanic plumes to invert for the co-eruptive rate of energy release. By applying it to a unique dataset of submarine tephra dispersal from an MOR eruption [15] we conduct the first inversion of dispersal data from a submarine tephra deposit. Our results yield direct predictions for the energy transfer rate associated with co-eruptive plume-driven tephra transport and show that the dispersal of tephra over the km-scale distances commonly observed at deep marine volcanic settings requires a rapid syn-eruptive energy transfer. The resultant total co-eruptive energy release aligns precisely with independent oceanographic constraints on both the volume and energy contents of megaplumes, providing conclusive evidence that megaplume formation can occur synchronously with the explosive (or tephra-generating) phase of deep-sea eruptions, likely over a period of hours. Our direct inference of the *rate* of energy release also provides new inroads for scrutinizing proposed sources of megaplume energy.

[56]

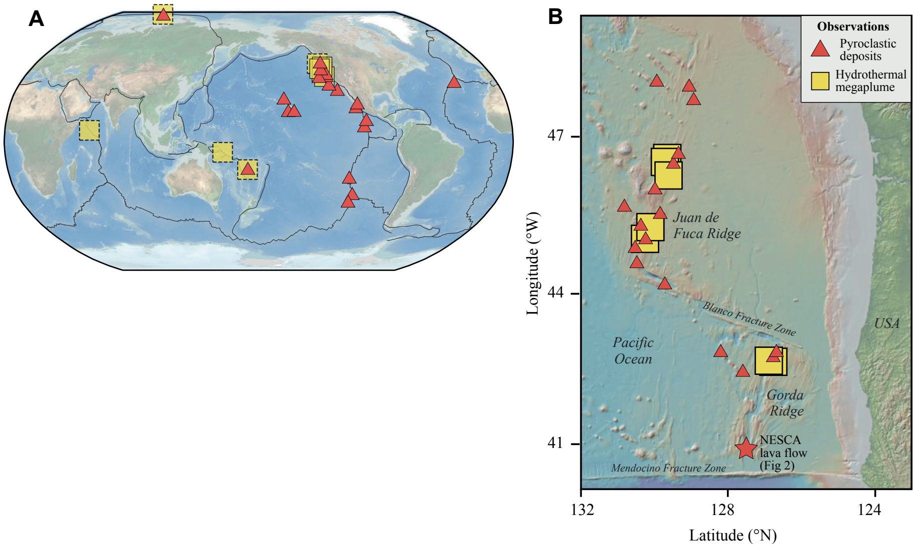

Figure 1: **Observations of hydrothermal megaplumes and deep-marine tephra deposits (A) globally and (B) in the NE Pacific.** Locations of megaplumes detected by water-column measurements (yellow boxes) and observed deep-marine pyroclastic tephras (red circles). Boxes with solid lines show plumes that have been mapped in three dimensions and therefore have known volumes ($\sim$10-150 km$^3$; 7 observations), while dashed lines indicate those with chemical and physical characteristics consistent with a megaplume but without a confident volume estimate (5 observations). Deep-marine tephras have been discovered in multiple locations at both MORs and seamounts. These encompass the global range of MOR spreading rates and water depths of up to 4 km. The preponderance of observations in the NE Pacific (shown in (B)) is related to the concentration of marine research in this region. The location of the eruption and tephra deposit used for our inversion (Fig. 2) is shown by the star symbol in (B)). Tephra observations, particularly in (B), are from [15] with additional data from [18–26]. Megaplume observations are from compilations by [5, 6]. Black lines in (A) show tectonic plate boundaries.

## Submarine pyroclastic deposits

Observations made over the last decade have shown that fragmental volcanic deposits are a common feature of deep-marine magmatic settings. Imaging and sampling of the seafloor at ridges [15, 18, 19, 25] and seamounts [20–22, 26, 28–31] has revealed the presence of tephra over many km$^2$, typically comprising sub-cm shards of volcanic glass. Dispersal distances for these tephras are inferred to reach several km. Older tephra-bearing sediments recovered from sediment cores taken on the flanks of MORs also indicate similar dispersal scales [23, 24]. Although some debate exists on whether these tephras are generated primarily via magmatic fragmentation of fluid magma [15] versus other brecciation processes such as thermal granulation [32] or hydrovolcanic fragmentation [31], many authors have interpreted these deposits as evidence for explosive volcanism occurring in the deep ocean [15, 19], something that has traditionally been considered extremely rare due to the high hydrostatic pressure [33]. Indeed,

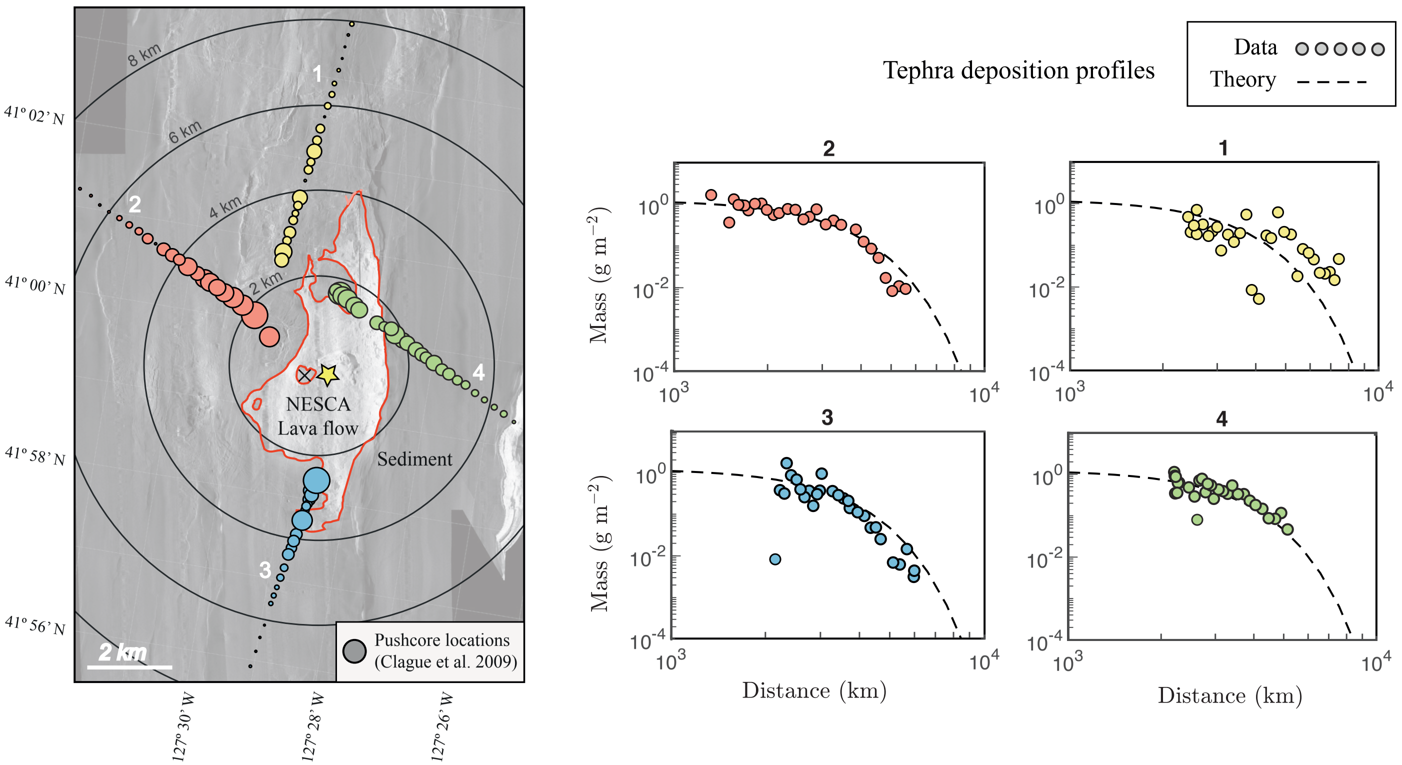

Figure 2: **Map and tephra deposition pattern at the NESCA eruption site with theoretical fits.** (A) Sidescan sonar imagery of the NESCA lava flow at the southern end of the Gorda Ridge (see Fig. 1A). Circles show locations of sediment pushcores taken along four profiles around the flow by [15], with the area of the data points proportional to the mass per unit area of tephra in the 250-500 μm range. The extent of the lava flow is indicated by a red outline. (B) Mass per unit area of the corresponding sampled data profiles (labeled 1-4) as a function of distance from an inferred center marked by the yellow star in the map. The inferred center is the unique position creating a global minimum in mean square error resulting from fitting our Guassian model given by Eqn. (1) to the data. This is approximately 800 m from the location of the actual eruptive vent, recently identified using high-resolution bathymetric data (D. Clague, pers. comm.) and shown by the black cross. The Gaussian dispersal pattern resulting from our regression analysis is shown as a dashed curve on each of the plots, for which the dispersal scale $L \approx 4.9$ km. The 15% error in estimating the mass of glass particles [15] corresponds to the approximate size of the circular markers. Concentric circles in (A) represent 2-km increments from the calculated center. Sonar imagery from [27].

explosive eruption styles have now been directly witnessed at water depths exceeding 500 m at submerged arc [34, 35] and rear-arc [36] volcanoes, demonstrating that explosive deep-marine pyroclastic eruptions do indeed occur. Regardless of the precise mechanism of clast generation, observations have shown that the creation and dispersal of both silicic and basaltic tephra is common during eruptions in the deep ocean, particularly along the mid-ocean ridge system [15, 19, 23–25]. However, with the exception of the pyroclastic deposit studied here (sampled and mapped by [15]), no detailed information exists on the distribution of submarine tephras around their source eruptive vent or fissure, the location of which is typically unknown. As such, the development of an explanation for the primary mechanism of tephra dispersal, as well as the assessment of the possibility to invert submarine depositional patterns for paleo-eruptive properties (as is routinely attempted for subaerial tephras [37]), have remained unexplored to date.

## DISPERSAL MECHANISM

### Tephra deposit and dispersal characteristics

In this study we formulate a model of particle dispersal by a hydrothermal plume, demonstrate that its predictions are consistent with observations of submarine deposits, and apply it to invert directly for the energy discharge rates produced during a submarine eruption. This application is possible owing to the existence of a unique dataset of tephra deposition from a single isolated submarine eruption, the basaltic NESCA lava flow [27], collected by D. Clague and co-workers [15] in the Northern Escanaba Trough at the Gorda Ridge, NE Pacific (Fig. 2A). The lava and tephra from this eruption (estimated to have been emplaced around 300 years ago) are the only volcanic deposits in this region that overlie the sediments deposited by the Missoula floods [38]. Pyroclasts up to 1 mm in size were sampled and mapped around the lava flow via pushcores collected by a remotely operated vehicle, revealing lateral transport distances exceeding 5 km in all directions. The tephra particles were separated into different size fractions and the relative mass of each fraction measured. The plots in Fig. 2B show the mass distribution of pyroclasts in the 250-500 $\mu$m range along each of four profiles of pushcore data from [15] (the central position used to define the zero distance, shown as a yellow star in Fig 2A, will be discussed later in our analysis). In all cases, the mass of material decreases with distance from the source with an approximately axisymmetric, qualitatively Gaussian thinning trend.

It has been suggested that the km-scale lateral transport of submarine tephras may be a consequence of vertical lofting above the eruptive vent, followed directly by settling within a sustained cross current [39]. Depending on location, the background flow in the deep sea can be anticipated to form from a superposition of deep ocean currents, tidal currents, mesoscale eddies, internal waves and turbulent mixing (e.g. breaking internal waves). In view of the near-axisymmetric form of the observed dispersal at NESCA, we can anticipate that advection in a sustained cross flow is highly unlikely. Otherwise, the dispersal would be preferentially skewed in one direction. The lack of a dominant effect of sustained cross flows in the NESCA ash deposit is consistent with the absence of significant focused oceanic currents in the NE Pacific (month-long speed averages in this region of the deep ocean are $< 0.006$ m s$^{-1}$ [40]). Like the ash deposition pattern, strong oceanic currents would, in analogy with subaerial umbrella plumes, produce a slender, near-linear plume (and corresponding deposition field) in the direction of the background crossflow. Sustained unidirectional currents may nonetheless affect tephra dispersal within the specific areas of the ocean containing deep-ocean currents forming part of the global ocean circulation. Tidal currents could, in principle, produce a radial-like dispersal owing to their periodicity; however, by considering the trajectories of particles in a typical tidal field (see section 3 of the Supplementary Methods), we determine that tidal reversal constrains the transport of tephra by tidal currents to a maximum distance of $700$ m from the eruptive source. The much larger dispersal radii of $> 5$ km observed in all directions at NESCA cannot therefore be explained by advection within either deep-ocean currents nor tidal currents.

We propose instead that the characteristics of the observed tephra deposition suggest a dominant transport mechanism by buoyancy-driven advection within the *umbrella* of a syn-eruptive hydrothermal plume, forming a gravity current spreading radially along a neutral level of the density stratified ocean. For an effectively quiescent ambient ocean, the umbrella would remain approximately axisymmetric during the tephra dispersal phase, advecting particles laterally by its own buoyancy-driven flow while maintaining the particles in suspension within turbulent eddies. The heavy tephra particles progressively fall out of the suspension of the turbulent flow to produce a thinning deposition of particles in all directions. This proposed mechanism is consistent with the observed near-axisymmetric, qualitatively gaussian thinning dispersal trends at NESCA, as well as observations of approximately ‘ellipsoidal’ megaplumes [6, 41]. While tephra transport in a buoyancy-driven plume umbrella is often considered in idealized prototypical fluid-mechanical analysis of tephra dispersal by subaerial eruptions [42, 43], it is neglected in standard methods for inverting subaerial tephra data, owing to the need for a new kind of mathematical model needed to account for horizontal buoyancy-driven flow. The most standard models and inversion toolkits designed for subaerial eruptions [44, 45] account for horizontal transport of particles via advection by atmospheric crosswinds and diffusive atmospheric mixing, but entirely neglect the advection by buoyancy within the plume umbrella. In situations where this approach is applied to near-axisymmetric subaerial eruptions, the method infers unphysical values for the atmospheric diffusivity [46], reflecting the fact that the dispersal in such cases can be dominated by buoyancy-driven flow in the plume umbrella [47]. In the submarine context, buoyancy-driven spreading is likewise the only mechanism that can account for substantial radial dispersal; even an upper bound on oceanic diffusive mixing near MORs of $\kappa \sim 10^{-3}$ m$^2$ s$^{-1}$ can account for at most a few 10s m of horizontal displacement during particle descent (using the diffusive lengthscale $\sqrt{\kappa t}$, where $t$ is a timescale of particle descent on the duration of days).

Having discounted other candidate mechanisms of dispersal, we propose that buoyancy-driven horizontal flow of the umbrella must provide the primary driver of the dispersal of the tephra. If this is the case, then the dispersal is driven primarily by the input of heat at the seafloor. In principle, it should therefore be possible to correlate tephra deposition distances

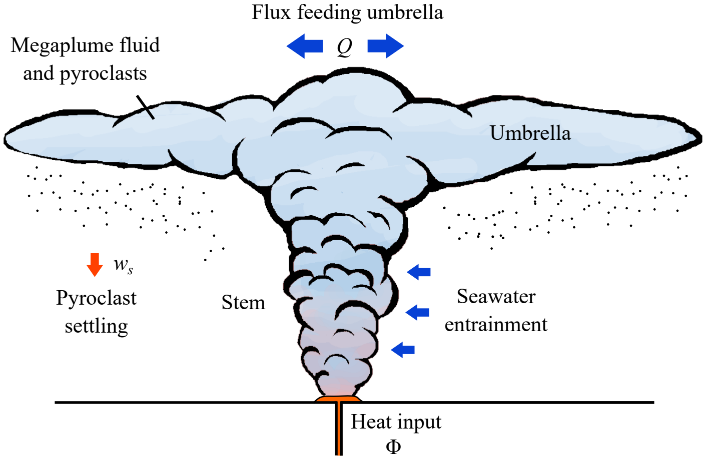

Figure 3: **Schematic showing the configuration and the processes controlling buoyancy-driven submarine tephra dispersal.** The hydrothermal plume forms a turbulent convecting stem fed by lava heating, and/or release of intracrustal fluid, which accumulates and cools following entrainment of ambient seawater. The stem feeds the neutrally buoyant umbrella, which forms a primarily horizontally flowing neutrally buoyant gravity current within the density stratification of the ocean, with a volumetric flux of $Q_{umb}$.

with energy input rates, yielding an inroad for the estimation of spatial, temporal and energetic characteristics of the heat discharge produced during volcanic eruptions. The analysis we present here demonstrates, we believe for the first time, that a model based on horizontal buoyancy-driven transport predicts the characteristics of a natural tephra deposit, and we develop the first inversion of data based on these transport dynamics.

## Tephra dispersal model and inversion method

An input of heat at the seafloor will coalesce into a vertically convecting column of heated water, herein referred to as the *stem* of the plume. This structure will both grow laterally and cool as it entrains ambient seawater [3] until reaching a neutral level at which the density matches that of the ambient stratification (Fig. 3). Following an inertial overshoot, the plume will settle along a neutral level as a turbulent, primarily horizontally flowing neutrally buoyant gravity current (or intrusion), forming the *umbrella* of the plume. Tephra produced during eruption of the lava will be carried by the plume stem into the umbrella, with some proportion of the tephra falling from the sides of the stem (a model predicting the tephra concentration through the stem of the plume and the proportion reaching the umbrella is developed in section 2 of the Supplementary Methods). On reaching the umbrella, the tephra will subsequently be transported primarily *horizontally* by buoyancy-driven flow within the umbrella, resulting in km-scale transport.

To develop our inversion methodology, we apply a model of the plume in two components,

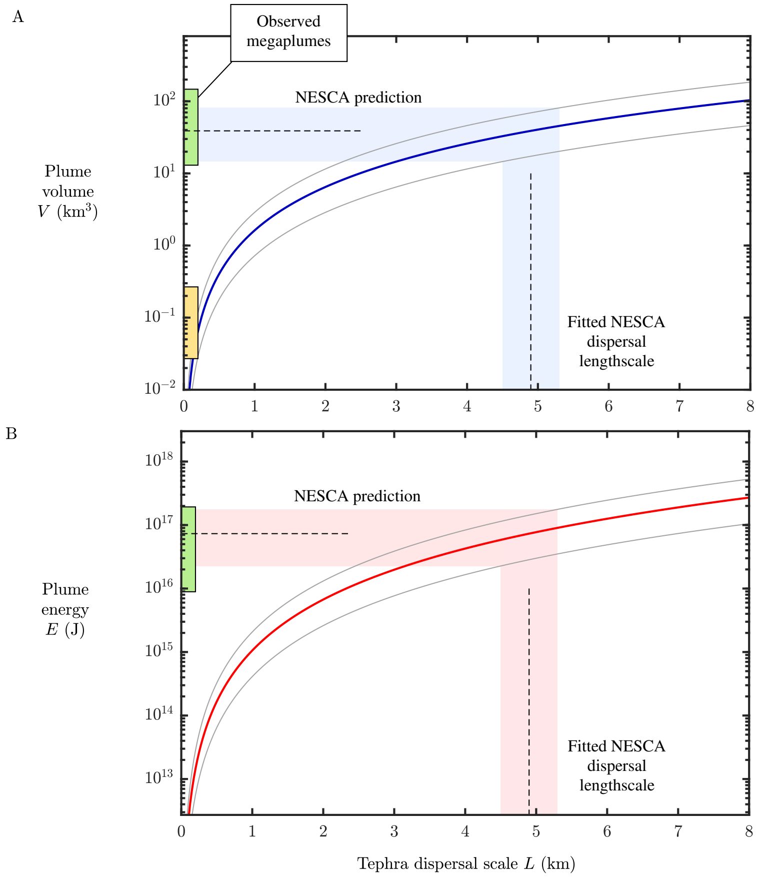

Figure 4: **The inversion results for plume umbrella volume and total energy and comparison with observed event plumes**. (A) The total volume and (B) total energy predicted by our model as functions of the observed tephra dispersal lengthscale ($L$), defined as the decay scale of the Guassian model of Eqn. (1) (and equal to the distance from the center encompassing $\sim$93% of the mass of tephra dispersed by the umbrella of the particle group under consideration). The value used for the Brunt-Väisälä frequency is $N = 10^{-3}$ s$^{-1}$ and the eruptive timescale used to convert our energy flux into a total energy is taken here as the representative value $\tau = 15$ hours (as derived in our results section, where a range of 10-20 hours is inferred based on the lava volume and morphology). The thick curves are evaluated for a settling speed of $w_s = 3$ cm s$^{-1}$, for the particle range 250-500 µm used in the inversion. The other curves (grey) represent the minimal and maximal inferences that would apply for settling speeds of $w_s = 2$ cm s$^{-1}$ and duration $\tau = 10$ hours, and $w_s = 4$ cm s$^{-1}$ and duration $\tau = 20$ hours, covering ranges of uncertainty in these parameters. Bands represent the inferred values based on the fitted dispersal length scale $L = 4.9 \pm 0.4$ km determined by our fitting to the observed data for the NESCA eruption (Fig. 2). The range of volumes and heat energies of observed megaplumes (volume $\geq 10$ km$^3$) [5] are indicated by the green bars along the vertical axes, showing consistency with both of our predictions. This indicates that a megaplume was produced during the NESCA eruption. The volume range of the considerably smaller group of event plumes observed at the Lau Basin [6] are indicated by the orange bar in (A), potentially forming a distinct category of event plume.

illustrated in Fig. 3. The stem of the plume is modeled as a turbulent, vertically convecting column of hot water, while the umbrella is modeled as a turbulent gravity current flowing along a neutral level of the ambient density stratification. The two regions are coupled by a condition of continuous volumetric flux between the top of the stem and the radial origin of the umbrella at the neutral buoyancy level. Particles entrained into the plume will, following possible fallout and recycling in the stem, propagate into the plume umbrella and settle from its base at a rate proportional to particle concentration [42, 43]. The theory of particle settling from axisymmetric gravity currents [42] predicts a Gaussian deposit profile:

$$\Omega(r) = \Omega_0 \exp\left[-\pi(r/L)^2\right], \tag{1}$$

where $\Omega(r)$ is the deposited particle mass per unit area of a group of particles (size range) characterized by a particle settling speed of $w_s$, $L = (Q_{umb}/w_s)^{1/2}$ is a lengthscale representing the scale on which the mass of the tephra group decays (encapsulating $\sim 93\%$ of the mass of deposited tephra of the particle group being considered), $Q_{umb}$ is the volume flux of fluid feeding the umbrella, and $\Omega_0$ is a constant representing the scale of accumulation (the total mass of tephra of the particle group being considered is $\Omega_0 L^2$). A review of the result of Eqn. (1) and derivation of the other components of our model below, are detailed in section 1 of the Supplementary Methods. The dispersal lengthscale $L$ is independent of both the duration of the eruption and the rate of input of particles (either of which will only accumulate $\Omega_0$) and hence $L$ provides an independent fitting parameter that can be used to constrain the volumetric flux sourcing the umbrella via the formula:

$$Q_{umb} = w_s L^2. \tag{2}$$

It should be noted that this inversion formula does not depend on the amount of tephra deposited (which is encapsulated in $\Omega_0$), and hence even a small particle input can be sufficient to apply it.

The model above is based on a number of assumptions. First, Eqn. (1) provides the deposition field under the assumption of a single (or representative) particle settling speed $w_s$. In our analysis, we will choose a specific particle range (extracted by sieving [15]) and assume a particle settling speed representing this group. Another assumption underlying the model is that the plume is sustained by an approximately steady buoyancy source over the eruptive duration. While a waning input rate can be anticipated under the various theories for megaplume creation, we can anticipate that an approximation of a constant input rate provides a representation of the averaged properties of the plume system during the main period of energy release. Attenuation of the source energy will provide a relatively smaller contribution to deposition at late times. A further assumption underlying the model is that the presence of particles does not significantly impact the fluid flow. By developing a model for particle transport in the stem of the plume in section 2 of the Supplementary Methods, we show that this is likely to be an excellent approximation for this application owing to the considerably larger proportion of plume fluid compared to particle mass.

By utilizing further mathematical models of the plume stem, we can relate the flux of heat energy sourcing the plume from the eruptive vent or fissure (whichever is the most appropriate source geometry for the eruption of interest) to the flux of fluid flowing into the umbrella, $Q_{umb}$, according to:

$$\Phi \approx \begin{cases} 0.187\,k\left(\dfrac{N^5 Q_{umb}^4}{\varepsilon^2}\right)^{1/3} & (l \lesssim l_*), \\ 0.326\,k\left(\dfrac{N^3 Q_{umb}^3}{\varepsilon l}\right)^{1/2} & (l \gtrsim l_*), \end{cases} \tag{3}$$

where $l$ is the source fissure length, $l_* = 3(\varepsilon Q_{umb}/N)^{1/3}$ is a lengthscale characterizing the fissure length on which the dynamics transition from axisymmetric to planar models, $\varepsilon \approx 0.1$ is the entrainment coefficient, $k \approx 2.1$ GW m$^{-4}$ s$^3$ is the conversion factor between buoyancy flux and heat flux, and $N$ is the Brunt-Väisälä frequency of the ocean stratification. With the flux reaching the umbrella $Q_{umb}$ determined from the first stage of our inversion represented by Eqn. (2), the formula above provides the rate of hydrothermal heat input $\Phi$ introduced at the base of the plume necessary to generate this flux.

## RESULTS

### Dispersal of the NESCA tephra

The observed profiles of tephra deposition for the NESCA flow are shown for four groups of pushcores in Fig. 2B, each forming an approximately linear path along the seafloor (Fig. 2A). The deposition profiles all follow qualitatively Gaussian decay trends. This provides support for our essential hypothesis that buoyancy-driven flow in the umbrella was the primary driver of the dispersal, as represented by the prediction of Eqn. (1). To estimate the dispersal scale $L$ and the center of the dispersal, $\boldsymbol{x}_c = (x_c, y_c)$, we determined the position $\boldsymbol{x}_c$ and values of $\Omega_0$ and $L$ (a total of four fitting parameters) that minimize the root mean square error:

$$E = \left(\frac{1}{N}\sum_{i=1}^{N}\left|\Omega_i - \Omega_0 \mathrm{e}^{-\pi|\boldsymbol{x}_i-\boldsymbol{x}_c|^2/L^2}\right|^2\right)^{1/2}, \tag{4}$$

where $\Omega_i$ and $\boldsymbol{x}_i$ denote the mass per unit area and positions of particles in the sampled range of 250-500 µm of the $N$ pushcores. This was achieved by conducting a grid search of positions $\boldsymbol{x}_c$ over a rectangular region surrounding the lava flow. For each position on the grid, $\boldsymbol{x}_c$, the root mean square $E$ was minimized over values of $\Omega_0$ and $L$ using a nonlinear programming solver. The unique position yielding the overall minimum error, $\boldsymbol{x}_c = (-127.4892, 40.9893)$, is indicated by the yellow star in Fig. 2A. The corresponding value of $L$ is $4.9$ km. Recently acquired high-resolution bathymetry of the NESCA flow (D. Clague, pers. comm.) has revealed that the eruption occurred from a ring-fault around a small sediment hill indicated by a cross in

Fig. 2A, located $\sim 800$ m from our inferred center. The proximity demonstrates the potential to identify source vents from tephra data.

The fitted model of Eqn. (1) determined from our global minimization is plotted alongside the data for each of the four pushcore groups in Fig. 2B. There is consistent general agreement between the data and the guassian trends, with 51% of the data lying above the model curve, and an $R^2$ value of $\sim 0.6$. Bootstrapping $10^4$ resampled datasets yields a standard deviation of 400 m in the fitted value of $L$. Since ours is a continuum model for the statistically averaged deposition field, deviations between our model and the data are expected. The scatter may represent syn- or post-depositional processes such as statistical noise in the turbulent and particle dynamics, the effect of topography (particles falling unevenly on sloped surfaces), sediment displacement and/or bioturbation, combined with a 15% predicted error in the measurement of the proportion of tephra in each pushcore [15] (indicated by the size of the markers in Fig. 2B). Clague *et al.* [15] observed that the majority of the tephra in their pushcore samples resided within the uppermost cm of the seafloor sediment, indicating that most of the sampled tephra had remained largely undisturbed since deposition. However, some particles had been mixed downwards by bioturbation, in some cases by up to 1 m, providing a source for outliers.

In addition to $L$, the other parameter required to complete our inversion for the umbrella flux using Eqn. (2) is a representative settling speed $w_s$ for the particle species used in our analysis (250-500 µm). For this, we use the general formula for particle settling speeds [48] with coefficients for settling tephra particles determined using tank experiments by [39] (see section 5 of the Supplementary Methods for details on these relationships). A representative settling speed for this group is $w_s \approx 3 \pm 1$ cm s$^{-1}$.

Using the inferred dispersal scale of $L = 4.9 \pm 0.4$ km and the representative settling speed of the group, $w_s \approx 3 \pm 1$ cm s$^{-1}$, the inversion formula of Eqn. (2), $Q_{umb} = w_s L^2$, predicts that the volumetric rate of growth of the umbrella was $Q_{umb} \approx (7.6 \pm 3.6) \times 10^5$ m$^3$ s$^{-1}$ $\approx (2.8 \pm 1.3)$ km$^3$ hour$^{-1}$. In turn, the implied rate of heat transfer at the hydrothermal source predicted by Eqn. (3) is $\Phi \approx (5.5 \pm 3.3) \times 10^{15}$ J hour$^{-1}$ or $1.5 \pm 0.9$ TW (assuming a point source or a fissure length $< 1$ km, which is most appropriate based on analysis of the NESCA bathymetry [49]; a source fissure longer than 1 km results in a slight decrease in the lower bound for the predicted energy flux; see Fig. 5 of the Supplementary Methods). In evaluating Eqn. (3), we used a value for the Brunt-Väisälä frequency $N \approx 10^{-3}$ s$^{-1}$ derived for the seafloor near the NESCA site using the dataset of [50] (see section 6 of the Supplementary Methods). These inferences of $Q$ and $\Phi$ present the first constraints on rates of umbrella growth and heat energy input derived from buoyancy-driven tephra-dispersal dynamics.

It is important to note that since the energy flux at the plume source is constrained via the dispersal data, it characterizes the rate of energy transfer occurring during the period of hydrothermal discharge that was coincident with the generation of tephra. Estimating the total energy content of this tephra-bearing plume therefore requires some knowledge of the likely duration of the pyroclastic phase of the eruption. Observations from multiple submarine volcanic locations show that deep-sea tephra deposits of the kind sampled at NESCA are consistently associated with lava morphologies produced during high-effusion rate eruptions (i.e. sheet-flows)

[15]. Conversely, low effusion rate pillow-lava forming eruptions do not appear to produce significant amounts of fragmental material [15]. Constructing a detailed facies architecture of the NESCA lava and resolving a precise eruption chronology will require analysis of high resolution mapping data (e.g. [51]), however it is possible to use existing observations to estimate the likely duration of the pyroclast-producing phase of the eruption. The NESCA lava exhibits both pillow-lava and sheet-flow morphologies [27], implying a range of effusion rates over the course of the eruption (most likely $\sim 10^1$-$10^2$ m$^3$ s$^{-1}$ [52, 51]). The higher effusion rate (sheet-flow forming) phase appears to have occurred first [27], as is common for basaltic eruptions [53, 51]. Based on visual seafloor observations, these flows are estimated to account for a third of the erupted material [27], corresponding to an erupted volume of approximately $1.5 \times 10^7$ m$^3$ (based on the total erupted volume given by [15]). Using a typical range of volumetric discharge rates for submarine sheet-flows of $\sim$200-500 m$^3$ s$^{-1}$ [51], we estimate the duration of this activity, and therefore the probable timescale over which the tephra bearing plume was formed, to be $\tau$ $\sim$10-20 hours. Using the volume flux $Q_{umb}$ and heat transfer rate $\Phi$ constrained by our model, this would produce a plume with a volume of $\sim$ 15-80 km$^3$ and containing $\sim$ 2-20$\times 10^{16}$ J of heat. These ranges both lie directly within the ranges of total volume and total energy contents from observations of megaplumes shown as green bars in Fig. 4. These results imply that a megaplume was generated synchronously with the eruption of lava and dispersed tephra during its radial propagation along a neutral buoyancy level. Although the period of plume formation at NESCA is somewhat uncertain, maintaining the energy flux necessary to disperse the tephra ($\sim$ 1-2 TW) over any reasonable eruptive period (hours to days) would produce a plume with physical characteristics within the range of observed megaplumes (Fig 4). Our conclusion that tephra dispersal must have occurred within a megaplume is not therefore strongly reliant on the precise timescale chosen. Our results support a direct causal link between active lava effusion, megaplume generation and the km-scale dispersal of tephra in the oceans.

## A direct volcanic origin for megaplumes?

A key controversy surrounding megaplumes is whether the energy that drives plume formation is supplied directly from cooling magma, either from seafloor lavas [14, 15] or in a subsurface dyke [16]), or alternatively is predominately sourced from the rapid evacuation of intracrustal hydrothermal systems [2, 54, 55]. The temporal-spatial correlation between several observed megaplumes and active/recent seafloor volcanism [4, 5, 9, 11] provides circumstantial evidence for a direct causal relationship between megaplume generation and eruptive activity. Our results support this association as they directly link megaplume formation and magma extrusion in both time and space. Debates on the feasibility of a volcanic/magmatic source have generally focused on the total energy contents of megaplumes as well as the origin(s) of the physico-chemical characteristics of megaplume fluids, such as $^3$He/Heat ratios and Fe and Mn concentrations [56, 57, 15, 12, 6, 58]. However, since neither the actual timescale of plume generation nor the precise temporal relationship with magma extrusion is known, these debates remain inconclusive. Since our model constrains the actual energy *flux* released during the eruption, independent from both the overall timescale of plume formation and total energy budget, we are able to advance this debate by taking the more direct approach of evaluating whether the *rate* of heat transfer expected from cooling lava and/or exsolved magmatic volatiles can create the necessary buoyancy flux at the plume origin.

Upon eruption, the outer layer of submarine lava is rapidly quenched to form a solid insulating crust. The initial quenching of this outer layer is relatively fast, with a 1 mm thick crust forming in $<1$ s [59]. The temperature at the lava-water interface, and therefore the heat flux to the water, decreases as this conductive boundary layer thickens until either the flow is completely solidified or steady conditions are attained (dependent on the flow thickness, the magma supply rate, etc.). For flow thicknesses of $\geq$2-3 m, theoretical calculations based on heat conduction predict that the first few days of cooling are characterized by a waning heat flux at the lava-water interface within the range of $10^3$-$10^4$ W m$^{-2}$ [60]. In order to create the observed tephra dispersal at NESCA via lava heating, the results of our inversion indicate that the integrated energy flux from the surface of the lava during megaplume generation must have been at least $\sim 1$ TW (and possibly up to 2 TW). A heat flux within the first day of cooling of order $10^4$ W m$^{-2}$ [60] would require $\sim 100$ km$^2$ of lava, almost a factor of seven higher than the *total* area of the NESCA eruption (estimated to be 15 km$^2$ [15]). Because our prediction of the total energy content within the megaplume scales directly with the assumed duration of hydrothermal discharge, the ratio between the total energy in the plume and that released by any given area of cooling lava during the period of plume formation is constant regardless of the duration of megaplume generation (assuming a constant value for the heat flux at the lava-water interface). For example, the energy transfer from the maximum 15 km$^2$ of lava at NESCA with the maximum heat flux of $10^4$ W m$^{-2}$ would always contribute $\sim 15$ % of the total energy of the plume formed, regardless of its total volume. This estimate is also likely to be a generous upper bound because it assumes both instantaneous eruption of the lava and sustainment of the initially highest heat flux as cooling proceeds. Heat loss from fragmented magma (pyroclasts) is more efficient than the cooling at the surface of a lava flow assumed in the estimate above, however for typical MOR eruptions the mass fraction of fragmental material appears to be so low (for example at NESCA it is estimated to $<1$ wt $\%$ [15]) that this cannot provide a significant source of heat. Given the typical areal extent of most submarine lava flows ($<10$ km$^2$), we can anticipate that heat transfer from erupted magma is unlikely to be the dominant mechanism of megaplume generation. An alternative proposition is that megaplume fluids can be created via heating of pore fluids along the edges of a dyke [16]. However, this process also requires a prolonged period of heat transfer ($>$ 10 days, even at high crustal permeabilities [16]) in order to create sufficient volumes of hydrothermal fluid and is therefore similarly unable to provide the heat transfer rate necessary to create the required buoyancy flux for tephra dispersal.

A further possibility for a direct volcanic origin for megaplumes is heating of seawater by a separate fluid phase composed of exsolved magmatic volatile species [15], similar to the formation of subaerial eruption plumes. Although volatile exsolution is relatively limited during seafloor eruptions (and MOR magmas are themselves typically volatile poor), some bubble growth is probably necessary to provide the buoyancy for eruptive ascent [33] and a $CO_2$ rich fluid phase is likely to be present in the erupting magma. The most $CO_2$ rich MORB magmas probably have initial dissolved $CO_2$ contents of $\sim 1.5$ wt% [61], which for a NESCA sized eruption would transport around $\sim 10^{15}$ J of heat (assuming an initial temperature of 1200 °C, complete $CO_2$ exsolution, and a specific heat capacity of $c_p = 1.3$ kJ kg$^{-1}$ K$^{-1}$ [62]), one to two orders of magnitude below that required to form a megaplume. However, if explosive eruptive styles do occur on the seafloor then it is likely they are driven by accumulations of $CO_2$ rich fluid that is added to the ascending melt during eruption, possibly from a foam layer at the roof of the subsurface magma reservoir [33, 15, 19, 63]. This eruptive mechanism presents the possibility of an enhanced $CO_2$ flux at the eruptive vent, sourced from degassed magma deeper in the system. An energy flux of $\sim 1$ TW would require a $CO_2$ flux of $\sim 10^6$ kg s$^{-1}$ (equivalent to $\sim 10^4$ m$^3$ s$^{-1}$ at the depth of the NESCA vent). While a $CO_2$ output of this magnitude may be viable for short periods, it seems unlikely that this could be sustained over the period of hours required for megaplume formation. Nevertheless, if megaplume generation is associated, at least partly, with volcanic energy release, then heat loss from exsolved $CO_2$ rich bubbles is a more realistic energy source than cooling magma. A direct input of exsolved magmatic volatiles may also provide a better explanation for some of the distinctive chemical features of megaplumes, such as their $^3$He/heat values, compared to magma-water interaction [57, 56, 15].

Based on the above analysis it seems probable that the rapidity of megaplume formation at NESCA, and probably elsewhere [6], cannot be easily achieved by volcanic processes alone and likely requires an additional syn-eruptive energy source. The most obvious mechanism for generating this energy flux is the rapid evacuation of pre-existing intra-crustal hydrothermal fluids triggered by the mechanical effects of dyke intrusion [2, 54, 55]. A crustal origin for at least a portion of megaplume fluids is consistent with the presence of (crustally-derived) thermophilic microbes observed in plume fluids at the Gorda Ridge in 1996 [64] and the high rates of energy transfer required for tephra dispersal suggests that these fluids may represent the dominant component of megaplumes. Seafloor eruptions that do not involve the concurrent release of significant volumes of crustal fluid, perhaps due to a lack of available fluids or magma ascent conditions that do not promote fluid discharge, should therefore produce substantially smaller plumes. The size of such plumes would be limited by the more restricted/short-lived energy transfer available from volcanogenic heating only. This may explain the formation of a series of event plumes of considerably smaller volumes $V < 0.5$ km$^3$ (indicated by the orange bar in Fig. 4 A) detected after an eruption in 2008 in the Lau Basin [6]. It is notable in this regard that megaplumes have so far only been observed, or suspected, above volcanoes in extensional tectonic settings (i.e. MORs and back-arc ridges; Fig. 1), where seafloor hydrothermal systems are commonplace and the extensional tectonic regime promotes hydrothermal circulation, which may be significantly enhanced by dyke intrusions [55]. Although future observations may yet document megaplumes associated with other submarine volcanic environments, it could be expected that syn-eruptive plumes in non-rift settings are typically less energetic. This inference could be tested by applying our inversion method to plume dispersed pyroclasts from other submarine volcanic settings (see below), such as submerged volcanic arcs (e.g. [28])

## Linking megaplumes, seafloor eruptions and tephra transport

The release of hot intracrustal fluid triggered by magma intrusion does not, in principle, necessitate an eruption. However it is notable that observed megaplumes are commonly associated with events involving lava extrusion [58] and appear to form directly above freshly emplaced lava flows [9]. It has also been noted that, on occasions when seafloor seismic events have not culminated in eruptions, no anomalous hydrothermal activity has been detected [58] (although the detection and observation of active seafloor eruptions remains extremely challenging). As demonstrated here, in the absence of strong unidirectional currents, achieving transport distances in excess of  1 km for even relatively small pyroclasts ($<500$ μm) requires a significant time-averaged energy flux close to the eruptive source of around 1-2 TW. Maintaining this heat flux for a period exceeding 5-10 hours would equate to a total energy release consistent with the observed heat contents of megaplumes ($10^{16}$-$10^{17}$ J), shown in Fig. 4B. The apparent ubiquity of widely dispersed submarine tephras (Fig. 1), and the aforementioned correlation between lava extrusion and megaplume detection, both indicate that syn-eruptive energy transfers of a magnitude comparable to that predicted for the NESCA eruption are an intrinsic characteristic of many volcanic events occurring in the deep oceans. In light of this, we anticipate that the processes leading to rapid intracrustal fluid release (i.e. dyke intrusion into the uppermost crust) will also generally produce lava extrusion, even though the energy transfer rate from erupted magma alone is unlikely to account for observed tephra transport distances of several km. It may also be the case that the interaction of ascending magmas with $CO^2$ rich foams is more prevalent during MOR eruptions than previously thought and that the initial phase of seafloor eruptions are often characterized by high rates of energy transfer via exsolved volatiles.

Finally, we note that our methodology of inversion based on tephra-transport within the umbrella of a hydrothermal plume can be anticipated to apply to general situations where the ambient is sufficiently quiescent that it is unable to compete significantly with the buoyancy-driven radial flow during particle dispersal, and the particle concentration is small enough such as not to significantly affect the fluid dynamics. Tephra transport from submarine eruptions can occur via other mechanisms, such as density currents generated by plume collapse [28, 35] or the advection of settling particles by ocean currents [39], however these will not produce radially dispersed deposits over length-scales of several km with Gaussian thinning trends (as are clearly apparent in the NESCA data; Fig. 2). While our analysis reveals primarily radial ash transport within a megaplume, our method is equally applicable to tephra transported by any eruptive plume, regardless of size or total energy content. In situations where background crossflow also contributes, our methodology could be generalized by comparing observed tephra depositions alongside a fluid-mechanical model of the umbrella suitably generalized to incorporate background flow and fitting for the background flow rate (if unknown) and flux feeding the umbrella simultaneously. The signature of the flux feeding the umbrella and, in turn, the heat flux at the seafloor origin, will manifest in the lateral buoyancy-driven expansion of the flow perpendicular to the direction of the crossflow.

## SUMMARY

In this work we have demonstrated, we believe for the first time, that the horizontal buoyancy-driven transport of tephra in a plume umbrella (in this case from a submarine deposit) can be used to constrain the energy discharge rates associated with volcanic eruptions. Our method presents a novel approach to invert tephra dispersal data for eruptive energetics. By applying this model to the submarine tephra deposit from the NESCA eruption, we have shown that km-scale tephra dispersal in the deep ocean can be explained by buoyancy-driven transport in a syn-eruptive megaplume and our results conclusively link megaplume generation with the tephra-generating phase of this eruption. The similarity between the NESCA tephra deposit and many other deep marine tephras (wrt. particle size, morphology, dispersal range etc.) suggests that this is a common occurrence during submarine eruptions at ocean ridges. Although our results demonstrate a clear temporal-spatial correlation between megaplume formation and seafloor eruptions, the primary energy source for megaplume creation seems unlikely to come directly from the erupted magma. While some portion of the heat transfer that drives megaplume creation must be derived from the concurrent volcanic eruption, via cooling magma and, probably more significantly, exsolved $CO_2$, it seems likely that the high rates of energy release required to transport submarine tephras are associated with the rapid evacuation of hydrothermal reservoirs [2, 6, 7], probably in response to dyke intrusion into the uppermost crust [55]. This inference can potentially be tested by future *in situ* observations of syn-eruptive hydrothermal processes [65] and continued sampling and chemical analysis of megaplume fluids. Application of our inversion method to paleo-tephra deposits recovered from marine sediment cores [23, 24] could, in principle, provide new inroads towards constraining the long-term ($\gtrsim$10 ka) time-averages of the flux of mass and heat from the crust to the oceans associated with seafloor volcanic events.

## Data availability statement

The data analyzed in this study is published in Ref 15.

## Code availability statement

Custom computer codes used to generate the results reported in this paper are available from the corresponding author upon reasonable request.

# SUPPLEMENTARY METHODS

## 1 Plume model and buoyancy-driven horizontal dispersal

The *stem* of the plume forms a turbulent column of hot water that propagates vertically within the ambient density stratification of the ocean. The turbulent flow in the stem of the plume will entrain ambient seawater, causing it to cool and eventually rise to a height where it is heavier than the ambient seawater. Following an inertial overshoot, the flow will settle along a neutral level, forming the *umbrella*. This second regime forms a turbulent, horizontally propagating flow known as an intrusion or neutrally buoyant gravity current [66]. The stem and umbrella are coupled by a condition of continuous volumetric flux $Q_{umb}$ between the top of the stem and the radial source of the umbrella at a neutral buoyancy level.

Particles entrained into the plume will, following possible fallout and recycling in the stem, propagate into the plume umbrella and sediment from its base at a rate proportional to particle concentration [42, 43]:

$$\frac{\partial(ch)}{\partial t} + \frac{1}{r}\frac{\partial}{\partial r}(rchu) = -w_s c, \tag{5}$$

where $c(r,t)$ is the volume concentration of particles, $r$ is the horizontal distance from the plume center, $h(r,t)$ is the thickness of the umbrella layer, $u(r,t)$ is the thickness-averaged horizontal velocity of the flow, and $w_s$ is the settling speed of the particle species being considered. The right-hand side represents the rate of particle fallout, which is modeled as proportional to the concentration and the settling speed [42, 43, 67, 68]. Time-dependent numerical analysis of the fully time-dependent gravity-current equations [66] shows that the current extends along a near-steady envelope. Consequently, the condition of uniform flux $2\pi rhu \equiv Q_{umb}$ applies to excellent approximation in Eqn. (5) during the growth of the umbrella. Using this expression to substitute for $hu$ in Eqn. (5) and integrating the resulting equation for $c$, one obtains the Gaussian prediction for the spatial profile of the mass per unit area of ash deposited per unit time, $\Omega = \rho_b c$ where $\rho_b$ is the density of the basaltic glass, given by

$$\Omega(r) = \Omega_0 \mathrm{e}^{-\pi(r/L)^2}, \tag{6}$$

where $L = (Q_{umb}/w_s)^{1/2}$ is referred to as the umbrella dispersal lengthscale, and $m_0$ is the integration constant. The result of Eqn. (6) applies downstream of the radius of the plume stem, $r_0$. Assuming that the settling particles are not significantly advected from their fallout position (consistent with the assumption of an approximately quiescent ambient), Eqn. (6) provides the deposition profile of tephra along the seafloor. The constants $\Omega_0$ and $L$ form the only two parameters defining the dispersal pattern (Eqn. (6)) and describe two independent degrees of freedom associated with purely buoyancy-driven particle dispersal. The constant $\Omega_0$ represents the accumulation of the dispersal pattern, related to the rate of particle generation and source duration (a larger eruptive duration will accumulate a larger mass per unit area but the dispersal profile will retain the same shape as it accumulates). The parameter $L$ independently represents the radial rate of decay of the deposition profile, and contains information of the rate of fluid input into the umbrella $Q_{umb}$ and the settling speed $w_s$ representing the particle size under consideration. The axisymmetric dispersal pattern described by Eqn. (6) decays monotonically with a smooth tail in all directions from the plume center. With the dispersal lengthscale $L$ inferred by fitting Eqn. (6) to an observed tephra deposition profile, the volumetric flux feeding the umbrella can then be inferred using the formula

$$Q_{umb} = w_s L^2. \tag{7}$$

Since $L$ is independent of both the duration of the eruption and the rate of input of particles (either of which will only accumulate $\Omega_0$), $L$ independently constrains the information of the volumetric flux sourcing the umbrella via Eqn. (7). Hence, even a small input of particles can, in principle, be sufficient to conduct our inversion. To invert for $Q_{umb}$, it remains only to estimate the settling speed of the particle under consideration $w_s$ and the dispersal length $L$ for the observed deposition distribution.

In the analysis above, it has been assumed that the particle species is represented by the same settling speed $w_s$. Volcanic tephra will naturally involve a polydisperse distribution. As discussed in section 4, the deposition field resulting from a polydisperse distribution can, under our assumption of a dilute suspension (see section 2), be represented as an integral superposition of Gaussians of the form (6), in which the integrand is weighted by a mass distribution function representing the concentration of particles as a function of particle size $d$. To apply our inversion, we choose a group of particles in the size range $[d - \delta d/2, d + \delta d/2]$ and assign a representative settling speed $w_s$ corresponding to the central value $d$. The data of [15] was partitioned using sieving into four categories, and we use the particle range containing the most number of particles, 250-500 µm, for our analysis. A representative range of settling speeds for this range is given by $w_s = 3 \pm 1$ cm s$^{-1}$ (see section 5), which we assume in our analysis.

The second step of our inversion predicts the heat energy $\Phi$ inputted into the hydrothermal plume at its base necessary to produce the volumetric flux $Q_{umb}$ feeding the umbrella at the top of the stem. The transfer of heat energy, either from inputted hot fluid or heating by lava, produces plume fluid through the process of entrainment of ambient seawater caused by the turbulent upwelling of the plume [3]. If the seafloor heat input is localized along a fissure, then a linear heat input is most appropriate. If the length of the source is sufficiently long (a prediction for how long will be determined below), a planar model of the plume stem may be most appropriate [3, 17]. If the fissure length $l$ is sufficiently short (and/or the intensity of the eruptive source sufficiently centralized), then the finitude of the source (edge effects) will invalidate the assumption of planarity. A point-source model will then ‘take over’ as being the more applicable. We develop models of both of these limiting endmember cases, and compare their predictions together. It should be noted that, irrespective of the geometry of the stem, it is clear from the characteristics of the NESCA deposition profile (Fig. 2), particularly its conformity with Gaussian axisymmetric dispersal, that the umbrella was primarily radially spreading (as opposed to primarily one-dimensional flow perpendicular to a fissure strike, for example, which would create an exponential, as opposed to guassian, decay in only the two horizontal directions perpendicular to the fissure). Predominately radial flow of the umbrella at the large scale is possible despite potential sourcing by a planar seafloor origin, either because the flow of the umbrella will lose information of the details of its source geometry beyond a characteristic distance due to lateral buoyancy-driven spreading, and/or because the stem will approach an axisymmetric plume during ascent (for sufficiently short fissure lengths). In either case, we propose a 'hybrid' model in which either a predominantly axisymmetric or planar seafloor source feeds the approximately radially spreading umbrella assumed above.

In the limit of an axisymmetric stem, we apply the model of a vertically flowing plume given by [69], as specified by

$$\frac{\mathrm{d}Q}{\mathrm{d}z} = 2\sqrt{\pi}\varepsilon M^{1/2}, \qquad \frac{\mathrm{d}M}{\mathrm{d}z} = \frac{FQ}{M}, \qquad \frac{\mathrm{d}F}{\mathrm{d}z} = -N^2 Q, \tag{8}$$

where $z$ is the vertical coordinate with respect to the seafloor, $N$ is the Brunt-Väisälä frequency, $\varepsilon \approx 0.1$ is the entrainment coefficient, and $Q(z)$, $M(z)$ and $F(z)$ are the volume, momentum and buoyancy fluxes, respectively. It should be noted that the model above describes only the predominantly vertically flowing stem of the plume, and does not apply in the neutrally buoyant umbrella for which the earlier model of Eqn. (5) applies. Let $F_0$ denote the buoyancy flux introduced at the base of the plume. By considering the intrinsic scalings of Eqn. (8) and $F \sim F_0$, we determine the unique intrinsic flux scale in the system as $Q_* = \left(\varepsilon^2 F_0^3/N^5\right)^{1/4}$. Solving Eqn. (8) numerically using a Runge-Kutta integrator subject to the heat-source condition $F = F_0$ and $Q = M = 0$ at $z = 0$, we determine the prefactor to this intrinsic scale giving the explicit formula for the flux at the top of the plume: $Q_{umb} = 3.52\, Q_* = 3.52\left(\varepsilon^2 F_0^3/N^5\right)^{1/4}$. This provides the desired relationship between the input of buoyancy at the seafloor $F_0$ and the flux feeding the umbrella $Q_{umb}$. On rearranging this expression for the source buoyancy flux $F_0$, we obtain

$$F_0 = 0.187 \left(\frac{N^5 Q_{umb}^4}{\varepsilon^2}\right)^{1/3}, \tag{9}$$

which provides the buoyancy flux needed to generate the flux $Q_{umb}$ feeding the umbrella at the top of the plume stem. Thus, once $Q_{umb}$ has been determined from the first stage of our inversion, the expression above represents the second stage to infer the source buoyancy flux.

Under the assumption of a planar stem applicable to sufficiently long fissures, we consider the two-dimensional analogue of the model of Eqn. (8) specified by:

$$\frac{\mathrm{d}q}{\mathrm{d}z} = -2\varepsilon\frac{m}{q}, \qquad \frac{\mathrm{d}m}{\mathrm{d}z} = \frac{fq}{m}, \qquad \frac{\mathrm{d}f}{\mathrm{d}z} = -N^2 q, \tag{10}$$

where $q$, $m$ and $f$ represent the volume flux, momentum flux and buoyancy flux per unit width of the fissure, and $\varepsilon$ is the entrainment coefficient [3]. We assume that the plume is sourced by a buoyancy flux per unit length $f_0 = F_0/l$, where $F_0$ is the total source buoyancy flux and $l$ is the fissure length. In this model, it is assumed that the fissure is long enough that edge effects from the ends of the fissure are negligible (the condition for this assumption to apply yo good approximation will be discussed below). similarly as we did for the axisymmetric model, we conduct a scaling analysis of the equations above to obtain the prediction for the fluid flux per unit length at the top of the stem: $q_{umb} = 2.11\,(\varepsilon f_0^2)^{1/3}/N$, where we use a numerical solution to determine the dimensionless prefactor. Recasting this expression in terms of the total source buoyancy flux and the umbrella volume flux using $f_0 = F_0/l$ and $q_{umb} = Q_{umb}/l$, and rearranging for $F_0$, we obtain

$$F_0 = 0.326 \left( \frac{N^3 Q_{umb}^3}{\varepsilon l} \right)^{1/2}, \tag{11}$$

forming the planar analogue of Eqn. (9). For a given umbrella flux $Q_{umb}$, the buoyancy flux $F_0$ predicted by Eqn. (11) decreases with fissure length $l$ because a longer source produces a larger surface area along the sides of the plume, creating more efficient entrainment. If a detailed numerical or experimental study of plumes generated by finite line sources were conducted, then the results above can be expected to provide $l \to 0$ and $l \to \infty$ asymptotes. Since the planar theory will breakdown for sufficiently small fissure lengths and the relevant theoretical prediction will switch to the axisymmetric endmember (the axisymmetric theory represents a theoretical upper bound as $l \to 0$). The predictions of the models of Eqn. (9) and (11) are equivalent at a fissure length of

$$l_* = 3.0 \left( \frac{\varepsilon Q_{umb}}{N} \right)^{1/3}, \tag{12}$$

which characterizes the fissure length on which the transition between the theories occurs. The two predictions are illustrated together in Fig 5, where we have assumed the values of $N = 10^{-3}$ s$^{-1}$ and $Q_{umb} = (7.6 \pm 3.6) \times 10^5$ m$^3$ s$^{-1}$, with a dashed curve showing the anticipated transition between the two theories predicted by Eqn. (12).

Finally, we convert the inferred buoyancy flux at the source into a flux of heat energy using the expression $\Phi = kF_0$, where $k \equiv \rho c/\alpha g$ is the conversion factor between buoyancy flux and heat flux, $\rho$ is the density of seawater, $c$ is the specific heat capacity, $\alpha$ is the coefficient of thermal expansion, and $g$ is the acceleration due to gravity. Combining this with the two expressions for $F_0$ above, we obtain

$$\Phi \approx \begin{cases} 0.187\,k \left( \dfrac{N^5 Q_{umb}^4}{\varepsilon^2} \right)^{1/3} & \text{(axisymmetric, } l \lesssim l_*\text{)}, \\ 0.326\,k \left( \dfrac{N^3 Q_{umb}^3}{\varepsilon l} \right)^{1/2} & \text{(planar, } l \gtrsim l_*\text{)}. \end{cases} \tag{13}$$

A typical value for the conversion factor is $k \approx 2.1$ GW m$^{-4}$ s$^3$, using values of $\rho \approx 1027$ kg m$^{-3}$, $c \approx 4200$ J kg$^{-1}$ K$^{-1}$, $\alpha \approx 2.1 \times 10^{-4}$ K$^{-1}$ and $g \approx 9.8$ m s$^{-2}$. Having determined the volumetric flux into the umbrella $Q_{umb}$ using the first stage of our inversion using Eqn. (7), the result of Eqn. (13) provides the flux of heat energy introduced into the plume system at its seafloor origin necessary to produce this flux.

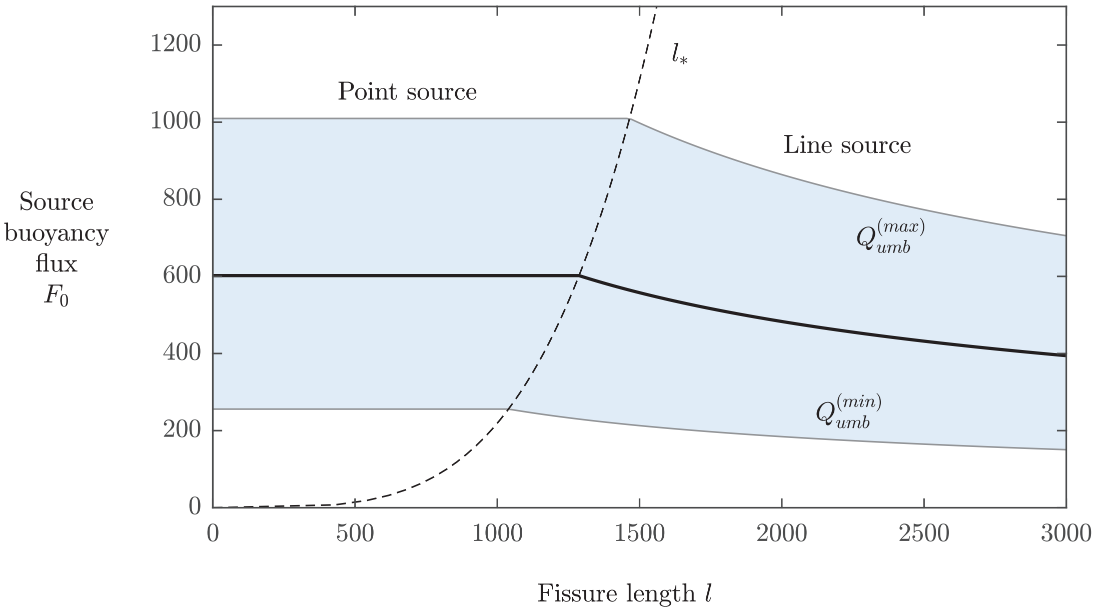

Figure 5: **Inferred buoyancy flux as a function of fissure length, illustrating the transition from a point-source model for the plume stem to a line-source model.** The blue shading represents the range of inferred values of the buoyancy flux at the plume source $F_0$ given the full range of umbrella fluxes, $Q_{umb}^{(min)} < Q_{umb} < Q_{umb}^{(max)}$, predicted by Eqn. (2), as a function of the length of the source $l$. For a point source, or sufficiently small fissure lengths $(l \lesssim l_*)$, the details of the source are unimportant to good approximation and the predictions conform to those of a point-source model, as given by Eqn. (9). For sufficiently long sources $(l \gtrsim l_*)$, a model assuming a planar source becomes more applicable in accordance with the prediction of Eqn. (11). The lengthscale $l_*$, given by Eqn. (12) and indicated by a dashed curve, represents the fissure length on which the two theories are equivalent.

## 2 Tephra transport dynamics in the stem and the conditions for dominant umbrella dispersal

This section develops theoretical conditions for umbrella dispersal to occur. This is done first by considering a necessary condition for significant umbrella dispersal, namely, that the dispersal distance predicted by the dynamics of the umbrella is considerable larger than the radius of the plume stem. Second, we develop a theory for the characteristic 'rise height' of particles in the stem of the plume. By comparing this to the neutral level of the plume, we determine a condition for a significant proportion of particles to reach the umbrella. The two conditions derived are found to involve the same key dimensionless parameter $\Gamma = w_s/(NF_0)^{1/4}$.

### Condition for umbrella dispersal

A necessary condition for significant dispersal by the umbrella is that the umbrella dispersal scale $L$ is larger than the maximum radius of the plume stem, $r_0$. As a metric to assess the satisfaction of this condition, we define the umbrella dispersal parameter:

$$\Lambda \equiv L/r_0, \tag{14}$$

representing the ratio of the umbrella dispersal length scale $L$ to the maximum stem radius $r_0$. If $\Lambda \gg 1$, then the umbrella-driven dispersal considerably exceeds the maximum distance that can be dispersed by the stem, which is consistent with the former being the dominant process. Conversely, if $\Lambda \ll 1$, dispersal cannot extend beyond the stem radius and will be limited to settle below the plume stem. To determine $\Lambda$ in terms of the intrinsic parameters specifying the plume-particle system ($F_0$, $N$ and $w$), we substitute the relationships for $L$ and $r_0$ given by our theoretical model of section 1 above. First, we recall from Eqn. (7) that $L = (Q_{umb}/w_s)^{1/2}$ and from the text below Eqn. (8) that $Q_{umb} = 3.52(\varepsilon^2 F_0^3/N^5)^{1/4}$. To estimate $r_0$, we use the expressions for the cross-sectional area and radius of the stem given by $A = Q^2/M$ and $r(z) = \sqrt{A/\pi}$ in accordance with the top-hat form of the model of [69]. From scaling analysis and a numerical integration of Eqn. (8), we can estimate the maximum radius of the stem to be $r_0 \approx \varepsilon(F_0/N^3)^{1/2}$. Substituting these expressions into Eqn. (14), we determine the umbrella dispersal parameter given by Eqn. (14) as a function of the intrinsic parameters:

$$\Lambda \approx 3\left(\frac{F_0 N}{w_s^4}\right)^{\frac{1}{8}} \equiv 3\,\Gamma^{-1/2}. \tag{15}$$

The result reveals the key dimensionless parameter grouping $\Gamma = w_s/(F_0 N)^{1/4}$ controlling the relative significance of umbrella dispersal. Appreciable umbrella dispersal ($\Lambda \gtrsim 1$) will occur for $\Gamma \lesssim 10$. Thus, larger plume buoyancy fluxes (larger $F_0$) and stronger stratifications (larger $N$) result in relatively more dispersal through the umbrella. For characteristic values of $F_0 \approx 600$ m$^4$ s$^{-3}$, $N \approx 10^{-3}$ s$^{-1}$ and $w_s \approx 3$ cm s$^{-1}$ arising in our analysis of the 250-500 µm particle range in the NESCA eruption, we obtain $\Gamma \approx 0.034$, and hence $\Lambda \approx 16$, consistent with significant distances of dispersal via the umbrella.

### Umbrella versus stem dispersal

We develop here also a model to predict the proportion of particles reaching the umbrella. To do this, we begin by generalizing a theory of Ernst *et al.* [70] describing the particle concentration in a plume stem to the case of a general plume and stratification. Following [70], we describe the particle mass concentration, $c(z,t)$, using the particle conservation equation:

$$\frac{\partial}{\partial t}(Ac) + \frac{\partial}{\partial z}(Qc) = -w_s(2\pi r)c, \tag{16}$$

where $A(z)$ is the horizontal cross-sectional area of the plume, is the plume radius, $Q(z)$ is the volume flux of the plume, as determined by Eqn. (8), and the right-hand side represents the rate of particle fallout. In essence, Eqn. (16) is the analogue of Eqn. (5) for the stem. In these definitions and Eqn (16), the functions of $Q(z)$ and $M(z)$ are known *a priori* from the solution to the model of Eqn. (8). Using the expressions for the area and radius, $A = Q^2/M$ and $r(z) = \sqrt{A/\pi}$, Eqn. (16) can be rewritten as

$$\frac{\partial}{\partial t}\left(\frac{Q^2 c}{M}\right) + \frac{\partial}{\partial z}(Qc) = -2\sqrt{\pi} w_s M^{-1/2}(Qc). \tag{17}$$

In steady state, Eqn. (17) forms an ordinary differential equation for the vertical mass flux of particles, $P(z) = Q(z)c(z)$, which we integrate to yield

$$P(z) = P_0 \exp\left(-2\sqrt{\pi} w_s \int_0^z M(\tilde{z})^{-1/2}\, \mathrm{d}\tilde{z}\right), \tag{18}$$

where $P_0$ is a constant of integration representing the inputted mass flux of particles (at $z = 0$). The result provides the required vertical distribution of particles for any given plume solution (any $Q(z)$ and $M(z)$ determined *a priori* from Eqn. (8)). For the case of a pure plume in a constant stratification, we write the momentum flux and the vertical coordinate in terms of their non-dimensional counterparts by $M(z) = (F_0/N)\hat{M}(\hat{z})$ and $z = (F_0/\varepsilon^2 N^3)^{1/4}\hat{z}$, giving

$$\hat{P}(\hat{z}) = \exp\left(-\beta\Gamma \int_0^{\hat{z}} \hat{M}(\bar{z})^{-1/2}\, \mathrm{d}\bar{z}\right), \tag{19}$$

where $\hat{P} = P/P_0$ is the normalized mass flux of particles ($\hat{P} = 1$ represents the input flux at $\hat{z} = 0$), $\beta = 2\sqrt{\pi/\varepsilon} \approx 11.2$ is a dimensionless prefactor and $\Gamma = w_s/(F_0 N)^{1/4}$ is the same intrinsic dimensionless number that appeared in Eqn. (15) above. The result of Eqn. (19) provides the flux of particles in the stem as a proportion of the flux inputted at the base. Evaluating Eqn. (19) at the top of the stem ($\hat{z} = 1.37$), we determine the proportion of particles reaching the umbrella:

$$\hat{P}_{umb} = \exp(-b\Gamma), \tag{20}$$

where $b \approx 33.7$, on using the fact that $\int_0^{1.37} \hat{M}(\bar{z})^{-1/2}\, \mathrm{d}\bar{z} \approx 3.0$. As shown by the plot of the relationship between $\hat{P}$ and $\Gamma$ given by Eqn. (20) in Fig. 6, the dimensionless number $\Gamma$ dials between situations where the vast majority of particles reach the umbrella ($\hat{P}_{umb} > 0.9$ for $\Gamma < 0.003$) to those in which the majority of particles fall from the umbrella ($\hat{P}_{umb} < 0.1$ for $\Gamma > 0.07$). Again, the dimensionless number $\Gamma$ has appeared as the key index for determining whether a given plume will disperse a particle species of settling speed $w_s$ primarily via the umbrella versus the stem. For $\Gamma \approx 0.034$, as predicted for the 250-500 μm particle range for the NESCA eruption (see subsection above), the result of Eqn. (20) indicates that 32% of the particles in the range of 250-500 μm will reach the umbrella. Thus, while significant dispersal of these particles reaching the umbrella will occur (in accordance with the condition derived

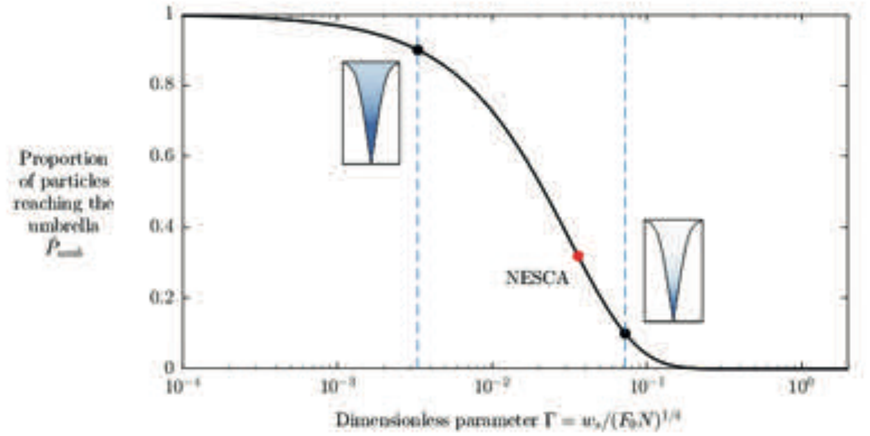

Figure 6: **Theoretical model for the proportion of particles reaching the umbrella of the eruptive plume.** The prediction for the proportion of particles reaching the umbrella given by Eqn. (20) as a function of the key dimensionless number $\Gamma = w_s/(F_0N)^{1/4}$. The result shows that over 90% of particles reach the umbrella if $\Gamma < 0.003$ and under 10% reach the umbrella if $\Gamma > 0.07$. Insets illustrate the concentration field of the plume $c(z) = \hat{P}(z)/\hat{Q}(z)$ predicted by Eqn. (19), with darker blue shading representing a higher concentration. The red filled circle represents the value predicted for the NESCA eruption for the particle range $250$-$500$ µm using our inferred values of $F_0 \approx 600$, $w_s = 3$ cm s$^{-1}$, for which $\sim 32\%$ of particles are predicted to reach the umbrella.

in the subsection above), our theory predicts a large proportion of the total number of particles introduced at the source of the plume will fallout from the sides of the stem. We therefore predict a considerable accumulation of tephra (likely more than 70% of the total mass of tephra produced) to have deposited near the vicinity of the source vent or fissure.

## Estimating tephra mass and concentration

We apply the model above to estimate the particle concentration throughout the plume system. In our analysis, we have assumed a single-phase model for both the stem and umbrella in which the presence of particles has a negligible effect on the fluid dynamics (producing a one-way coupling between the fluid dynamics and particle dynamics). This provides an excellent approximation if the mass concentration of particles is $< 10^{-3}$. The mass concentration of particles (the particle mass per unit fluid mass) is defined by

$$c = \frac{P(z)}{\rho Q(z)}, \tag{21}$$

where $P(z)$ is the flux of particle mass per unit horizontal cross-section (as predicted by the theory above), $\rho Q(z)$ is the flux of fluid mass and $\rho \sim 10^3$ kg m$^{-3}$ is the density of water. To estimate $P(z)$, we use the theoretical prediction of Eqn. (20) above. For the purpose of checking the self-consistency of our assumption of a single-phase model, we will assume a maximal particle flux using the estimate of the total mass of tephra $M = 2 \times 10^7$ kg (predicted by [15]) and the shortest duration for the tephra-producing stage of the eruption estimated in our results section ($\tau = 10$ hours), giving the mass flux of particles at the base of the stem as $P_0 \sim M/\tau \sim 500$ kg s$^{-1}$. Using the prediction for the particle mass distribution given by Eqn. (21), and the prediction for the volume flux of plume fluid, $Q(z) = (\varepsilon^2 F_0^3/N^5)^{1/4}\hat{Q}(\hat{z})$, we use Eqn. (21) to determine the mass concentration of particles as a function of height. The result shows that at least 99% of the stem has a particle mass concentration of $< 10^{-3}$, and that the particle mass concentration at the top of the stem (and hence through the umbrella) is $< 10^{-7}$. Single-phase models can therefore be expected to apply to excellent approximation for describing the dispersal from the umbrella (which will only decrease below this value due to the effects of radial spreading and particle fallout) and throughout the large majority of the stem.

## 3 Bounds on tidal dispersal

Continuous measurements from automated oceanic floats [71] show that tidal currents in the deep oceans form highly regular, symmetrical oscillations superposed with background noise, e.g. from eddies and internal waves. Due to the near-zero time average of tidal velocities over the course of a tidal cycle, both the settling of tephra and advection of the plume system will, under a purely tidal flow field, produce oscillations with a near-zero mean displacement. Hence, the total dispersal by tides is constrained to lie within a certain distance from the source representing the maximum distance a parcel is advected before the tide reverses. Material elements or particles released into a tidal field will undergo periodic, closed orbits in the vicinity of the vent. To show this, we compute the horizontal trajectories of fluid elements or particles, $[x(t), y(t)]$, advected under an illustrative tidal oscillation specified by

$$\dot{x} = U_x \cos\left(\omega t - \theta_x\right), \quad \dot{y} = U_y \cos(\omega t - \theta_y), \tag{22}$$

where $U_x$ is the maximum tidal current in the zonal direction, $U_y$ is the maximum tidal current in the meridional direction, $\omega$ is the frequency of the tidal oscillation, $\theta_x$ and $\theta_y$ are phase shifts, and the dot denotes a time derivative. Near the NESCA lava flow, the tidal currents reach magnitudes of approximately 5 cm s$^{-1}$ [71]. To simulate an illustrative tidal pattern, we set $\omega = 4\pi/T$, where $T$ is the duration of one day. Fig. 7A shows the dispersal pattern accumulated following the continuous composition of trajectories of parcels released continuously over the course of one day for an example: $U_x = 2$ cm s$^{-1}$, $U_y = 5$ cm s$^{-1}$, with $\theta_x = t_0\omega$ and $\theta_y = t_0\omega + \pi/2$. The pattern developed by tidal dispersal is confirmed to produce a closed region with an elliptical rim. To determine the rim position for general $\theta_x$, $\theta_y$, $U_x$ and $U_y$, we

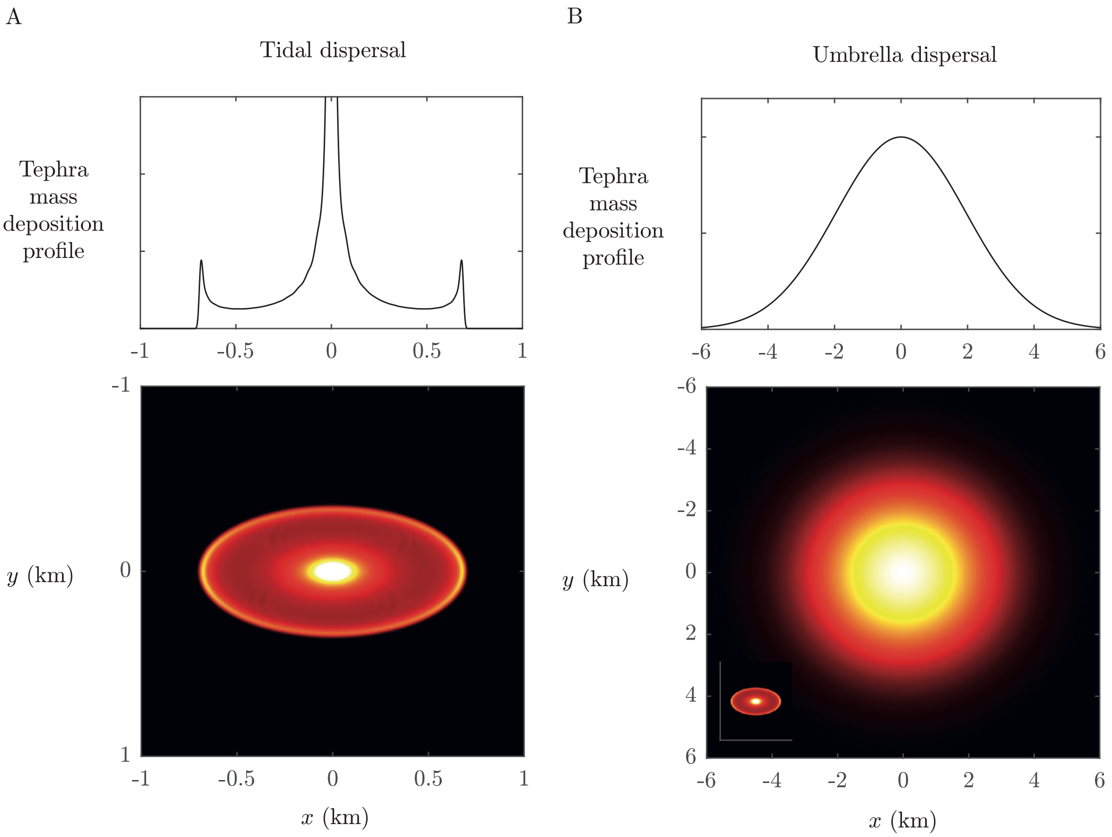

Figure 7: **Plan-views of the typical tephra deposition fields produced by tides or by buoyancy-driven lateral transport in the umbrella of the hydrothermal plume.** A characteristic dispersal field from (A) tidal advection and (B) advection within a buoyancy-driven umbrella, representing two endmembers for submarine tephra dispersal. Blue represents no particles, while yellow represents maximal deposited concentration. The tidal pattern (a) is given by superposing trajectories of particles released continuously over the course of one day predicted by the kinematic model of Eqn. (22), showing the maximum dispersal distance of $L_{tide}$ by tidal oscillation. The buoyancy-driven pattern (b) is given by the prediction of Eqn. (6). The case $L = 4.9$ km is illustrated for (b), corresponding to the dispersal distance inferred by fitting the deposition profiles for NESCA (Fig. 2). Upper panels show cross-sections of the dispersal patterns, illustrating the fundamentally different decay characteristics and dispersal distances operating under the two mechanisms. Panel (b) shows the tidal dispersal on the same scale as an inset, illustrating its considerably smaller scale.

integrate Eqn. (22) subject to the initial release position $(0, 0)$, giving

$$x = \frac{U_x}{\omega}\left[\sin(\omega t - \theta_x) + \sin\theta_x\right], \tag{23}$$

$$y = \frac{U_y}{\omega}\left[\sin(\omega t - \theta_y) + \sin\theta_y\right], \tag{24}$$

describing elliptical trajectories. The rim of the tidal dispersal pattern is the locus of maximum radii arising as $t_0$ is varied over one tidal cycle. The maximum distance of a particle released at $t = t_0$ occurs at $t = t_0 + \pi/\omega$. Substituting this value into (23) and (24), we determine the rim position parametrised as a function of $t_0$, given by

$$R(t_0) = \frac{2}{\omega}\left[U_x^2 \cos^2(\omega t_0) + U_y^2 \cos^2(\omega t_0 - \Delta\theta)\right]^{1/2}, \tag{25}$$

where $\theta_x = \omega t_0$ and $\Delta\theta = \theta_y - \omega t_0$. Since $0 \le \cos^2 \le 1$, it follows that the maximum dispersal distance is bounded by $L_{tide} = 2U/\omega = UT/2\pi$, where $U$ is the larger of $U_x$ and $U_y$. Mixed diurnal and semi-diurnal patterns can be modeled by superposition of two patterns of the form of Eqn. (22) with one frequency twice the other. This would result in more complex patterns than purely elliptical, but are likewise constrained by the maximum tidal distance of $L_{tide}$, with $U$ the maximum tidal speed in any given direction. For typical tidal currents in the NESCA region estimated from Argo floats [71], $U \lesssim 5$ cm s$^{-1}$, and hence $L_{tide} \lesssim 0.7$ km. In the absence of buoyancy-driven expansion of the umbrella, the independent effect of tides is thus to advect the plume-particle system back and forth within a radius of oscillation $L_{tide}$.

In addition to the closure of the orbit, a notable characteristic of purely tidal dispersal is the development of a sharp local maximum at the 'rim' of the tephra deposition pattern, evident in Fig. 7A (at least for a pure diurnal or semi-diurnal pattern; mixed tides, as apply in the NE Pacific, will produce a more complex pattern, though a similar constraint on the orbit will apply). This phenomenon is a consequence of the lingering of the trajectories near the rim as they switch direction during tidal reversal. Another characteristic is the non-axisymmetric eccentricity of the tidal dispersal pattern, which will generally arise for $U_x \neq U_y$ and $\theta_x \neq \theta_y$.

The deposition of tephra around the NESCA lava of more than 5 km in all directions is considerably larger than the maximum tidal dispersal scale $L_{tide} \sim 0.7$ km. In view of this, tidal advection cannot account for the observed deposition pattern at NESCA. We therefore propose instead that the dispersal was instead driven predominantly by buoyancy-driven radial flow of the umbrella along a neutral level, as detailed in section 1.

# 4 Approximation of a polydisperse deposition

In our analysis, we choose a representative settling speed $w_s$ for the group of particles we consider ($d = 250$-$500$ µm) and apply the monodisperse theory of Eqn. (7). To understand the strength of this approximation in a given situation, we consider here a generalized theoretical description of particle deposition allowing for a polydisperse distribution and use it to determine the strength of approximation of assuming a representative settling speed for a subset of particle settling speeds. Since the concentration of particles is highly dilute (see section 2), the total mass of deposited tephra per unit area of the seafloor $\Omega(r)$ at a distance from the source $r$ by the weighted integral superposition:

$$\Omega(r) = \int_0^\infty F_0(d) \mathrm{e}^{-\pi[r/L(d)]^2}\,\mathrm{d}d \equiv \int_0^\infty F(d,r)\,\mathrm{d}d, \tag{26}$$

where $F_0(d)$ is a weighting function (with units of mass per unit areas per unit particle size), $F(d, r)$ denotes the integrand, $L(d) = \sqrt{Q_{umb}/w_s(d)}$ is the dispersal lengthscale for the particle species of size $d$, $w_s(d)$ is the settling speed of the particle of size $d$ (see section 5 for a discussion of this relationship), and $F(d, r)$ is the density function (defined as the integrand).

In conducting our inversion for the umbrella flux $Q_{umb}$, we apply a monodisperse approximation to the particle range $250 < d < 500$ µm. The deposited mass per unit area for this group is represented by the truncation:

$$\Omega(r) = \int_{d_0-\delta d}^{d_0-\delta d} F_0(d) \mathrm{e}^{-\pi[r/L(d)]^2} \, \mathrm{d}d, \tag{27}$$

where $d_0 = 325$ µm is the central value and $\delta d = 125$ µm. By expanding the integrand about the central value, evaluating the integrals, and noting that the first order correction evaulates to zero, we obtain the approximation:

$$\begin{aligned} \Omega(r) &\approx 2\delta d F(d_0, r) + \tfrac{1}{3}\delta d^3 F_{dd}(d_0, r) && (28) \\ &\approx \Omega_0 \mathrm{e}^{-\pi[r/L(d_0)]} + O(\delta d^3), && (29) \end{aligned}$$

where $\Omega_0 = 2\delta d f(d_0)$.

# 5 Particle settling speeds

In order to determine a representative settling speed for this category, we utilized the relationship of [48] incorporating the coefficients for pyroclastic shapes determined using tank experiments by [39] (see Fig. 8). For the size range 250-500 µm used in our inversion (corresponding to the deposition shown in Fig. 2), the range $v = 3 \pm 1$ cm s$^{-1}$ is representative.

# 6 Ocean density stratification

The vertical profile of the Brunt-Väisälä frequency $N$ from the seafloor near the NESCA site is shown in Fig. 9A, as measured by ARGO floats [50]. The blue profile corresponds to the data gathered at the location closest to the lava flow. The value of $N \approx 10^{-3}$ s$^{-1}$ is characteristic for the abyssal region. The surrounding 8 profiles are shown as black dots in panel B (on a horizontal grid with a spacing of 0.5 degrees). The profiles of $N$ for these additional 8 locations, shown as grey curves in panel A, all produce the same representative value of $N \approx 10^{-3}$ s$^{-1}$.

# References

[1] White, J. D., Smellie, J. L. & Clague, D. A. Introduction: A deductive outline and topical overview of subaqueous explosive volcanism. *Explosive subaqueous volcanism* **140**, 1–23 (2003).

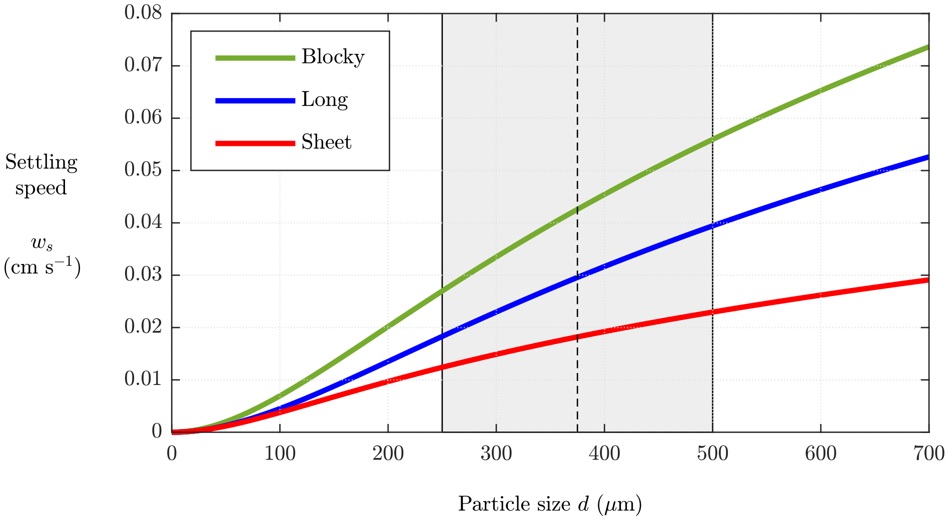

Figure 8: **Settling speed as a function of pyroclastic particle size.** The settling speed $w_s$ of three different types of clast are plotted against the particle size $d$, as predicted by the formula of [48] with the coefficients for basaltic tephra determined from tank experiments by [39]. The relationships are used to determine the characteristic settling speeds of the particles in the 250-500 µm range, shown shaded, used to conduct our inversion for the volumetric flux of fluid fed into the umbrella through Eqn. (7).

[2] Baker, E. T., Massoth, G. J. & Feely, R. A. Cataclysmic hydrothermal venting on the Juan de Fuca Ridge. *Nature* **329**, 149 (1987).

[3] Baker, E. *et al.* Episodic venting of hydrothermal fluids from the Juan de Fuca Ridge. *Journal of Geophysical Research: Solid Earth* **94**, 9237–9250 (1989).

[4] Embley, R., Chadwick, W., Perfit, M. & Baker, E. Geology of the northern Cleft segment, Juan de Fuca Ridge: Recent lava flows, sea-floor spreading, and the formation of megaplumes. *Geology* **19**, 771–775 (1991).

[5] Baker, E. T. *et al.* Hydrothermal discharge during submarine eruptions: The importance of detection, response, and new technology. *Oceanography* **25**, 128–141 (2012).

[6] Baker, E. T. *et al.* Unique event plumes from a 2008 eruption on the Northeast Lau Spreading Center. *Geochemistry, Geophysics, Geosystems* **12** (2011).

[7] Lupton, J. E., Baker, E. T. & Massoth, G. J. Helium, heat, and the generation of hydrothermal event plumes at mid-ocean ridges. *Earth and Planetary Science Letters* **171**, 343–350 (1999).

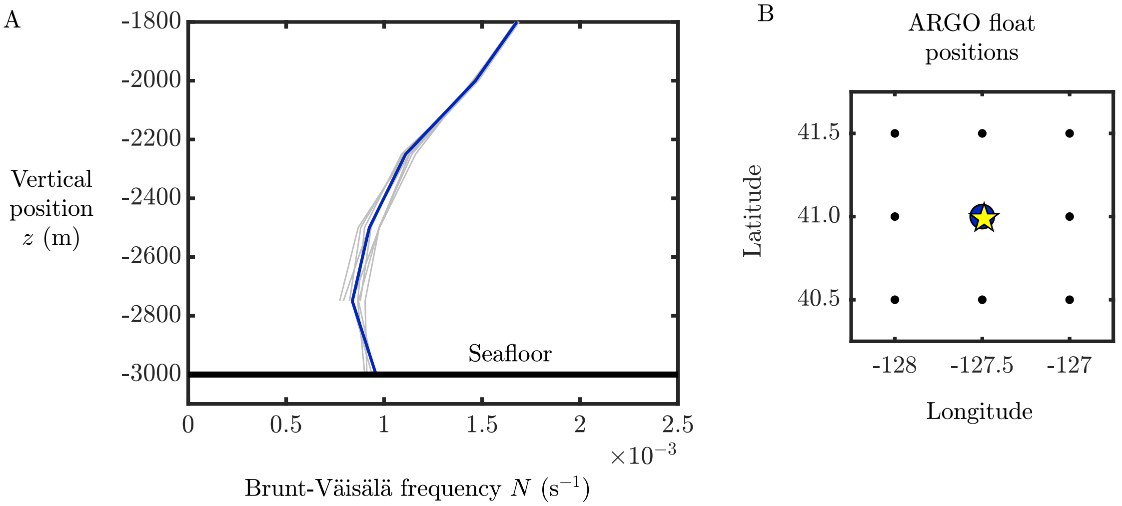

Figure 9: **Profile of the Brunt-Väisälä frequency $N$ as a function of height from the seafloor.** The profiles are provided by the dataset of [50]. Panel (A) shows the profile of $N = [-(g/\rho_0)\partial\rho/\partial z]^{1/2}$ as a function of vertical position, where $g \approx 9.8$ m s$^{-2}$ and $\rho_0 \approx 1027$ kg m$^{-3}$. The blue curve shows the profile closest to the NESCA lava flow. The profiles for the 8 surrounding profiles (on a grid with a resolution of 0.5 degrees) are also shown as gray curves, illustrating the near-uniformity of the profiles of $N$ over the entire region. The plots show that the value $N \approx 10^{-3}$ s$^{-1}$ characterizes the abyssal ocean, which we utilized in our inversion for the rate of heat transfer $\Phi$ in Eqn. (13). Panel B shows a plan-view of the sampled coordinates, with the position of the NESCA lava flow indicated by the yellow star.

[8] Murton, B. J., Baker, E. T., Sands, C. M. & German, C. R. Detection of an unusually large hydrothermal event plume above the slow-spreading carlsberg ridge: Nw indian ocean. *Geophysical research letters* **33** (2006).

[9] Baker, E. T. *et al.* Hydrothermal event plumes from the coaxial seafloor eruption site, juan de fuca ridge. *Geophysical Research Letters* **22**, 147–150 (1995).

[10] Baker, E. T. Patterns of event and chronic hydrothermal venting following a magmatic intrusion: new perspectives from the 1996 gorda ridge eruption. *Deep Sea Research Part II: Topical Studies in Oceanography* **45**, 2599–2618 (1998).

[11] Chadwick Jr, W. W., Embley, R. W. & Shank, T. M. The 1996 gorda ridge eruption: Geologic mapping, sidescan sonar, and seabeam comparison results. *Deep Sea Research Part II: Topical Studies in Oceanography* **45**, 2547–2569 (1998).

[12] Kelley, D. S., Lilley, M. D., Lupton, J. E. & Olson, E. J. Enriched H2, CH4, and 3He con-

centrations in hydrothermal plumes associated with the 1996 Gorda Ridge eruptive event. *Deep Sea Research Part II: Topical Studies in Oceanography* **45**, 2665–2682 (1998).

[13] Massoth, G. J. *et al.* Manganese and iron in hydrothermal plumes resulting from the 1996 Gorda Ridge Event. *Deep Sea Research Part II: Topical Studies in Oceanography* **45**, 2683–2712 (1998).

[14] Palmer, M. R. & Ernst, G. G. J. Generation of hydrothermal megaplumes by cooling of pillow basalts at mid-ocean ridges. *Nature* **393**, 643 (1998).

[15] Clague, D. A., Paduan, J. B. & Davis, A. S. Widespread strombolian eruptions of mid-ocean ridge basalt. *Journal of Volcanology and Geothermal Research* **180**, 171–188 (2009).

[16] Lowell, R. P. & Germanovich, L. N. Dike injection and the formation of megaplumes at ocean ridges. *Science* **267**, 1804–1807 (1995).

[17] Lavelle, J. The initial rise of a hydrothermal plume from a line segment source: Results from a three-dimensional numerical model. *Geophysical research letters* **22**, 159–162 (1995).

[18] Clague, D. A., Davis, A. S. & Dixon, J. E. Submarine strombolian eruptions on the gorda mid-ocean ridge. *Explosive subaqueous volcanism* **140**, 111–128 (2003).

[19] Sohn, R. A. *et al.* Explosive volcanism on the ultraslow-spreading Gakkel Ridge, Arctic Ocean. *Nature* **453**, 1236 (2008).

[20] Clague, D. A., Davis, A. S., Bischoff, J. L., Dixon, J. E. & Geyer, R. Lava bubble-wall fragments formed by submarine hydrovolcanic explosions on Lō'ihi Seamount and Kīlauea Volcano. *Bulletin of Volcanology* **61**, 437–449 (2000).

[21] Batiza, R., Fornari, D. J., Vanko, D. A. & Lonsdale, P. Craters, calderas, and hyaloclastites on young pacific seamounts. *Journal of Geophysical Research: Solid Earth* **89**, 8371–8390 (1984).

[22] Portner, R. A., Clague, D. A., Helo, C., Dreyer, B. M. & Paduan, J. B. Contrasting styles of deep-marine pyroclastic eruptions revealed from Axial Seamount push core records. *Earth and Planetary Science Letters* **423**, 219–231 (2015).

[23] Ferguson, D. J. *et al.* A 65 k.y. time series from sediment-hosted glasses reveals rapid transitions in ocean ridge magmas. *Geology* **45**, 491–494 (2017).

[24] Lund, D. C. *et al.* Anomalous Pacific-Antarctic Ridge volcanism precedes glacial termination 2. *Geochemistry, Geophysics, Geosystems* **19**, 2478–2491 (2018).

[25] Eissen, J.-P., Fouquet, Y., Hardy, D. & Ondréas, H. Recent MORB volcaniclastic explosive deposits formed between 500 and 1750 mbsl on the axis of the Mid-Atlantic Ridge, south of the Azores. *Washington DC American Geophysical Union Geophysical Monograph Series* **140**, 143–166 (2003).

[26] Maicher, D. & White, J. D. The formation of deep-sea Limu o Pele. *Bulletin of Volcanology* **63**, 482–496 (2001).

[27] Ross, S. L. & Zierenberg, R. A. Volcanic geomorphology of the SESCA and NESCA sites, Escanaba Trough. *Geologic, hydrothermal, and biologic studies at Escanaba Trough, Gorda Ridge, offshore northern California. US Geol. Surv. Bull* **2022**, 143–151 (1994).

[28] Murch, A. P., White, J. D. & Carey, R. J. Characteristics and deposit stratigraphy of submarine-erupted silicic ash, Havre volcano, Kermadec Arc, New Zealand. *Frontiers in Earth Science* **7**, 1 (2019).

[29] Walker, S. L. *et al.* Eruption-fed particle plumes and volcaniclastic deposits at a submarine volcano: Nw rota-1, mariana arc. *Journal of Geophysical Research: Solid Earth* **113** (2008).

[30] Carey, R. *et al.* The largest deep-ocean silicic volcanic eruption of the past century. *Science advances* **4**, e1701121 (2018).

[31] Schipper, C. I. & White, J. D. No depth limit to hydrovolcanic limu o pele: analysis of limu from lōihi seamount, hawaii. *Bulletin of volcanology* **72**, 149–164 (2010).

[32] Colombier, M. *et al.* In situ granulation by thermal stress during subaqueous volcanic eruptions. *Geology* **47**, 179–182 (2019).

[33] Head III, J. W. & Wilson, L. Deep submarine pyroclastic eruptions: theory and predicted landforms and deposits. *Journal of Volcanology and Geothermal Research* **121**, 155–193 (2003).

[34] Chadwick Jr, W. *et al.* Direct video and hydrophone observations of submarine explosive eruptions at nw rota-1 volcano, mariana arc. *Journal of Geophysical Research: Solid Earth* **113** (2008).

[35] Deardorff, N. D., Cashman, K. V. & Chadwick Jr, W. W. Observations of eruptive plume dynamics and pyroclastic deposits from submarine explosive eruptions at NW Rota-1, Mariana Arc. *Journal of Volcanology and Geothermal Research* **202**, 47–59 (2011).

[36] Resing, J. A. *et al.* Active submarine eruption of boninite in the northeastern Lau Basin. *Nature Geoscience* **4**, 799–806 (2011).

[37] Bonadonna, C. & Phillips, J. C. Sedimentation from strong volcanic plumes. *Journal of Geophysical Research: Solid Earth* **108** (2003).

[38] Normark, W. R. & Reid, J. A. Extensive deposits on the pacific plate from late pleistocene north american glacial lake outbursts. *The Journal of Geology* **111**, 617–637 (2003).

[39] Barreyre, T., Soule, S. A. & Sohn, R. A. Dispersal of volcaniclasts during deep-sea eruptions: Settling velocities and entrainment in buoyant seawater plumes. *J. Vol. and Geo. Res.* **205**, 84–93 (2011).

[40] Smith, C. A., Compo, G. P. & Hooper, D. K. Web-based reanalysis intercomparison tools (writ) for analysis and comparison of reanalyses and other datasets. *Bulletin of the American Meteorological Society* **95**, 1671–1678 (2014).

[41] D'Asaro, E., Walker, S. & Baker, E. Structure of two hydrothermal megaplumes. *Journal of Geophysical Research: Oceans* **99**, 20361–20373 (1994).

[42] Sparks, R. S. J., Carey, S. N. & Sigurdsson, H. Sedimentation from gravity currents generated by turbulent plumes. *Sedimentology* **38**, 839–856 (1991).

[43] Sutherland, B. R. & Hong, Y. S. D. Sedimentation from particle-bearing plumes in a stratified ambient. *Phys. Rev. Fluids* **1**, 074302 (2016).

[44] Bonadonna, C. *et al.* Probabilistic modeling of tephra dispersal: Hazard assessment of a multiphase rhyolitic eruption at Tarawera, New Zealand. *Journal of Geophysical Research: Solid Earth* **110** (2005).

[45] Barsotti, S., Neri, A. & Scire, J. S. The VOL-CALPUFF model for atmospheric ash dispersal: 1. Approach and physical formulation. *Journal of Geophysical Research: Solid Earth* **113** (2008).

[46] Volentik, A. C., Bonadonna, C., Connor, C. B., Connor, L. J. & Rosi, M. Modeling tephra dispersal in absence of wind: Insights from the climactic phase of the 2450 BP Plinian eruption of Pululagua volcano (Ecuador). *Journal of Volcanology and Geothermal Research* **193**, 117 – 136 (2010).

[47] Costa, A., Folch, A. & Macedonio, G. Density-driven transport in the umbrella region of volcanic clouds: Implications for tephra dispersion models. *Geophysical Research Letters* **40**, 4823–4827 (2013).

[48] Ferguson, R. & Church, M. A simple universal equation for grain settling velocity. *Journal of Sedimentary Research* **74**, 933–937 (2004).

[49] Clague, D. A. (2020). Personal communication.

[50] Gouretski, V. & Koltermann, K. P. WOCE Global Hydrographic Climatology. *Berichte des BSH* **35**, 1–52 (2004).

[51] Clague, D. *et al.* High-resolution auv mapping and targeted rov observations of three historical lava flows at axial seamount. *Oceanography* **30** (2017).

[52] Griffiths, R. W. & Fink, J. H. Solidification and morphology of submarine lavas: A dependence on extrusion rate. *Journal of Geophysical Research: Solid Earth* **97**, 19729–19737 (1992).

[53] Harris, A. *et al.* Effusion rate trends at Etna and Krafla and their implications for eruptive mechanisms. *Journal of Volcanology and Geothermal Research* **102**, 237–269 (2000).

[54] Cann, J. & Strens, M. Modeling periodic megaplume emission by black smoker systems. *Journal of Geophysical Research: Solid Earth* **94**, 12227–12237 (1989).

[55] Curewitz, D. & Karson, J. A. Geological consequences of dike intrusion at mid-ocean ridge spreading centers. *GEOPHYSICAL MONOGRAPH-AMERICAN GEOPHYSICAL UNION* **106**, 117–136 (1998).

[56] Palmer, M. & Ernst, G. Comment on "Helium, heat and the generation of hydrothermal event plumes at mid-ocean ridges", by je lupton, et baker and gj massoth. *Earth and Planetary Science Letters* **180**, 215–218 (2000).

[57] Lupton, J., Baker, E. & Massoth, G. Reply to comment by mr palmer and ggj ernst on"helium, heat, and the generation of hydrothermal event plumes at mid-ocean ridges"by je lupton, et baker and gj massoth. *E&PSL* **180**, 219–222 (2000).

[58] Embley, R. W. & Lupton, J. E. Diking, event plumes, and the subsurface biosphere at mid-ocean ridges. *Washington DC American Geophysical Union Geophysical Monograph Series* **144**, 75–97 (2004).

[59] Gregg, T. K. & Fornari, D. J. Long submarine lava flows: Observations and results from numerical modeling. *Journal of Geophysical Research: Solid Earth* **103**, 27517–27531 (1998).

[60] Deschamps, A. *et al.* Morphology and dynamics of inflated subaqueous basaltic lava flows. *Geochemistry, Geophysics, Geosystems* **15**, 2128–2150 (2014).

[61] Jones, M. *et al.* Quantitative vesicle analyses and total co2 reconstruction in mid-ocean ridge basalts. *Journal of Volcanology and Geothermal Research* **407**, 107109 (2020).

[62] Span, R. & Wagner, W. A new equation of state for carbon dioxide covering the fluid region from the triple-point temperature to 1100 k at pressures up to 800 mpa. *Journal of physical and chemical reference data* **25**, 1509–1596 (1996).

[63] Jaupart, C. & Vergniolle, S. The generation and collapse of a foam layer at the roof of a basaltic magma chamber. *Journal of Fluid Mechanics* **203**, 347–380 (1989).

[64] Summit, M. & Baross, J. A. Thermophilic subseafloor microorganisms from the 1996 North Gorda Ridge eruption. *Deep Sea Research Part II: Topical Studies in Oceanography* **45**, 2751–2766 (1998).

[65] Xu, G., Chadwick Jr, W. W., Wilcock, W. S., Bemis, K. G. & Delaney, J. Observation and modeling of hydrothermal response to the 2015 eruption at Axial Seamount, Northeast Pacific. *Geochemistry, Geophysics, Geosystems* **19**, 2780–2797 (2018).

[66] Johnson, C. G. *et al.* Modelling intrusions through quiescent and moving ambients. *Journal of Fluid Mechanics* **771**, 370406 (2015).

[67] Hazen, A. On sedimentation. *Transactions of the American Society of Civil Engineers* **54**, 45–88 (1904).

[68] Martin, D. & Nokes, R. Crystal settling in a vigorously convecting magma chamber. *Nature* **332**, 534–536 (1988).

[69] Morton, B. R., Taylor, G. I. & Turner, J. S. Turbulent gravitational convection from maintained and instantaneous sources. *Proc. R. Soc. Lond. A* **234**, 1–23 (1956).

[70] Ernst, G. G. J., Sparks, R. S. J., Carey, S. N. & Bursik, M. I. Sedimentation from turbulent jets and plumes. *Journal of Geophysical Research: Solid Earth* **101**, 5575–5589 (1996).

[71] Ollitrault, M. & Rannou, J.-P. ANDRO: an argo-based deep displacement dataset. *Journal of Atmospheric and Oceanic Technology* **30**, 759 – 788 (2013).